Modeling and Tracking of Heterogeneous Cell Populations via Open Multi-Agent Systems

A. Tramaloni[1], A. Testa[1], S. Avnet[2], S. Massari[2], G. Di Pompo[3], N. Baldini[2,3,#] and G. Notarstefano[1,#]

Abstract

Understanding cellular dynamics represents a critical challenge in biomedical research. Optical microscopy remains a key technique for observing live-cell behaviors *in vitro*. This paper introduces an enhanced cell-tracking algorithm designed to address dynamic changes in cell populations, including mitosis, migration, and cell-cell interactions, even within complex co-culture models. The proposed method involves three main steps: 1) modeling the movements and interactions of different cell types in co-culture experiments via tailored open multi-agent systems; 2) identifying parameters via real data for a multi-agent, multi-culture framework; 3) embedding the model within an Extended Kalman Filter, to predict the dynamics of heterogeneous cell populations across video frames. To validate the approach, we used a novel dataset which examines the interplay between tumor and normal cells, using osteosarcoma and mesenchymal stromal cells, respectively, as a model. This dataset offers a challenging and clinically relevant framework to track cell proliferation and study how cancer cells evolve and interact with stromal cells within their surroundings. Performance metrics demonstrated the algorithm effectiveness over state-of-the-art methodologies, highlighting its ability to track heterogeneous cell types, capture their interactions, and generate the estimated cell lineage tree.

Index Terms

Multi-Agent Systems, Filtering, Tracking, Osteosarcoma, Mesenchymal Stromal Cells, Systems Biology

I. Introduction

In recent years, the study of cells has gained interest in the control community. Recent works include [1]–[3]. The main idea behind these works is to leverage system theoretical approaches to model and control cell populations. These contributions span macro areas like cybergenetics [4] and multicellular systems modeling and simulation [5]. Relevant to our work is the application of multi-agent system paradigms to capture the emergent behaviors observed in heterogeneous cell populations, where individual cells can be modeled as interacting agents. Experimental data for these tasks are typically obtained from optical microscopy videos. Thus, to understand cell behaviors and their interactions, a preliminary task is to extract cell trajectories over time automatically. Biological cell tracking microscopy videos are thus becoming a fundamental task within broad application domains. Among the others, the tracking of tumour interaction with normal stromal cells *in vitro* is crucial to study tumor aggressiveness and drug resistance [6]. Among different techniques, optical microscopy is widely used to retrieve cellular images across different time instants [7].

Literature Review: We structure the literature review into three distinct sections. First, we review works focusing on cell tracking algorithms. Next, we discuss the application of (open) multi-agent concepts to systems and synthetic biology, as well as the inverse perspective, thus how tailored biological knowledge can be incorporated into multi-agent systems for applications beyond system biology, such as robotics. Finally, we explore systems theory and control approaches for analyzing and regulating the dynamics of cell populations. Multi-Cell Tracking (MCT) is a well-known problem in the literature, see, e.g., the surveys [8], [9] and references therein. Indeed, MCT arises in several application fields in biology, e.g., cybergenetics and drug discovery. Given this great interest in MCT, datasets and challenges have been proposed, such as the Cell Tracking Challenge, an established benchmark for MCT algorithms on *in vitro* monoculture experiments [10]. This study focuses on a novel co-culture dataset representing a new challenging scenario compared to other publicly available datasets.

We now introduce some current works on cell tracking algorithms. The method proposed in [11] combines convolutional neural networks (CNN) with recurrent neural networks for segmentation and tracking in microscopy images. A similar approach is presented in [12] where convolutional and long-short-term memory units are used to analyze cell motility data. Authors in [13] instead combine deep learning for cell segmentation and the so-called Viterbi algorithm for tracking. The study [14] proposes a multi-feature fusion re-tracking method using a Faster R-CNN network for detection. In [15], instead, the authors propose a graph neural network approach to model the entire time sequence of cells as a direct graph. The work in [16] proposes a single CNN for simultaneous cell segmentation and tracking to predict cell embeddings. A different approach is

This work was supported in part by the Italian Ministry of Foreign Affairs and International Cooperation, grant number BR22GR01, and by AIRC under the IG 2018—project ID 21403—to N.B. ("Altered lipid metabolism as a stress reaction to acid tumor microenvironment and a driver of metastasis in osteosarcoma").

# Equal contribution.

[1] Department of Electrical, Electronic and Information Engineering, University of Bologna, Bologna, Italy. {andrea.tramaloni, a.testa, giuseppe.notarstefano}@unibo.it.

[2] Department of Biomedical and Neuromotor Sciences, University of Bologna, Bologna, Italy. {sofia.avnet3, nicola.baldini5}@unibo.it, stefania.massari96@gmail.com.

[3] Biomedical Science, Technologies, and Nanobiotechnology Lab, IRCCS Istituto Ortopedico Rizzoli, Bologna, Italy. {nicola.baldini, gemma.dipompo}@ior.it.

presented in [17] where cell movements are predicted leveraging a Markov random field model and a spatial particle filter. In [18] the authors propose a variational joint local-global optical flow technique. These works do not explicitly model the cell population dynamics, often relying on black-box approaches that provide limited insights into local behaviors. In contrast, our approach integrates classical filtering methodologies with tailored multi-agent models, leveraging the dynamic interactions among cells to enhance motion prediction. Moreover, different from our approach, these works do not account for cell population heterogeneity. To the best of the authors' knowledge, existing methods have been developed only for monoculture experiments, whereas co-culture settings remain relatively uncommon.

Next, works connecting multi-agent system and systems biology are reviewed. Authors in [19] explore multi-agent modeling as a framework to design emergent collective behaviors in synthetic biology, focusing on multi-scale systems like synthetic cellularity and biological computation. Instead, the authors in [20] extend a spatially explicit agent-based model to study the entrainment and control of synchronized oscillating bacterial populations. Rather, the work in [21] applies systems biology concepts to networked controllers for coordinating multi-robot systems inspired by bacterial chemotaxis. Instead, for open multi-agent systems, the theoretical framework introduced in [22] provides a basis for studying live systems with time-varying state spaces. In this work, we build on similar concepts to model the dynamics of the considered living cell system, which is subject to population changes.

As for approaches to analyzing cell behaviors and modeling biological interactions, several works often leverage concepts from systems theory, identification, and control. For instance, in the work in [23], tumor cell behaviors are represented with ordinary, partial, or stochastic differential equations. However, these works do not focus on the dynamics of the single cell. The work in [24] discusses control schemes for gene regulation in cellular populations. Similarly, in [25] the authors propose the use of adaptive feedback control strategies to balance cell populations. The work in [3] models cancer treatment as a Stackelberg game between therapy and tumor evolution. The study in [2] considers the control of a cell population endowed with a bistable toggle switch. Moreover, the authors in [1] propose ratiometric control to regulate cell populations in synthetic toggle switches. The work in [26] introduces an eco-evolutionary model of cancer cells, analyzing how therapy-driven environments shape population dynamics. The authors in [27] developed an adaptive control method for state tracking in a nonlinear cancer-immune model, ensuring stability and effective tumor regulation. In these works, however, the focus is mainly on control schemes, while in our work we are interested in model design, identification, and cell behavior prediction. Differently from the above works, our paper proposes an identification procedure, exploiting real cell data, and a tracking scheme leveraging nonlinear multi-agent models that can capture interaction behaviors between the same or different cell types (normal and transformed cells).

Contributions: The contributions of this paper are as follows. We propose a novel algorithm called Heterogeneous Open Multi-Cell EKF-based Tracking (HEOM-EKF) for tracking cells in time-lapse experiments of *in vitro* co-cultures. The algorithm is designed by modeling heterogeneous cell populations as an open multi-agent system [28]. Specifically, we propose a class of open multi-agent models to predict biological cell dynamical behaviors while accounting for switches in the cell population dynamics over time, for instance, due to mitosis. Leveraging modeling tools from distributed systems, we capture cell-to-cell interactions involving state dependencies of neighboring cells, as, e.g., chemotaxis effects [29]. The considered models are not only able to capture the neighboring interactions among cells but also provide a framework to learn the behavior of interacting heterogeneous cell populations. Parameterized models are developed to capture different cell types, such as normal mesenchymal stem cells (MSC) and transformed osteosarcoma cells. We used these two cell types because, based on various studies—both our own and those of others over the past decades—it has become clear how crucial their interaction is in inducing aggressiveness and drug resistance in tumour cells [30]–[33]. Then, we propose ad-hoc system identification procedures to fit the considered models on real cell trajectories. Based on that, we develop a novel cell-tracking algorithm using an Extended Kalman Filter tailored to the identified open multi-agent model (HEOM-EKF), while also accounting for a time-varying number of cells. Thus, central to our approach is the recognition of cells as interacting agents rather than independent entities. This approach enabled us to redefine the EKF framework to reflect the collective state of the heterogeneous cell populations, thus allowing for more precise tracking of cellular ensembles and giving behavioral insights based on the learned model parameters. Within the algorithm, we also included a technique to estimate mitosis events and thus return the cell lineage tree at the end of the tracking procedure. Moreover, we construct a new annotated dataset from raw video data of *in vitro* cell experiments. Unlike most publicly available datasets, which focus solely on monoculture experiments, our dataset provides a unique resource for studying cellular behaviors in a co-culture framework. This dataset is designed not only for tracking purposes but also to support future research applications, serving as a challenging testing scenario involving different cell types.

A conference version appeared in [34]. In that preliminary study, the cell-tracking algorithm was designed for a monoculture scenario using a public dataset and relied on a standard multi-agent system formulation. In that preliminary setup, we did not take into account mitosis events, as well as cells entering and exiting the camera field of view. That is, the number of cells was assumed to be constant. In contrast, this journal version tackles a more challenging co-culture scenario and provides numerical results based on a private, unique dataset. This paper advances the methodology by employing an open multi-agent system that accommodates different agent types and supports dynamic cell population changes, thereby reflecting the considered heterogeneous cell populations. Moreover, the algorithm presented in this paper returns the cell lineage tree after tracking, thus providing deeper insights into cell interactions and evolution.

Paper Organization: The paper is organized as follows. In Section II, we introduce the cell-tracking problem and outline the essential components of multi-object tracking algorithms. Section III formalizes the open multi-agent system, generalized for multi-culture scenarios, and presents the parameter identification strategy. In Section IV, we describe the proposed HEOM-EKF algorithm. Section V provides an overview of the dataset construction with its further use for training and testing procedures, an analysis regarding the identified parameters of the multi-cell model, and finally presents numerical experiments that demonstrate the effectiveness of our algorithm through performance metrics.

II. Multi-Cell Tracking Problem Formulation

In this work, we consider a cell-tracking problem in a biological scenario in which the goal is to track multiple cells of different types in time-lapse sequences. Throughout the paper, we consider video frames in which the number of cells N^t changes over time. These variations may result from biological processes such as mitosis, and/or from cells entering or exiting the microscopy camera FOV.

In this section, we formalize the fundamental concepts behind cell-tracking algorithms. We will delve into more details in Section III, in which we model the cell population as an open multi-agent system and propose suitable formulations for their dynamics. These dynamical models will be a key component of the proposed cell-tracking strategy in Section IV.

The common elements that characterize cell-tracking algorithms typically include: $i)$ object detection, $ii)$ motion prediction, and $iii)$ data association. A schematic of this procedure is depicted in Figure 1. Object detection refers to the identification and

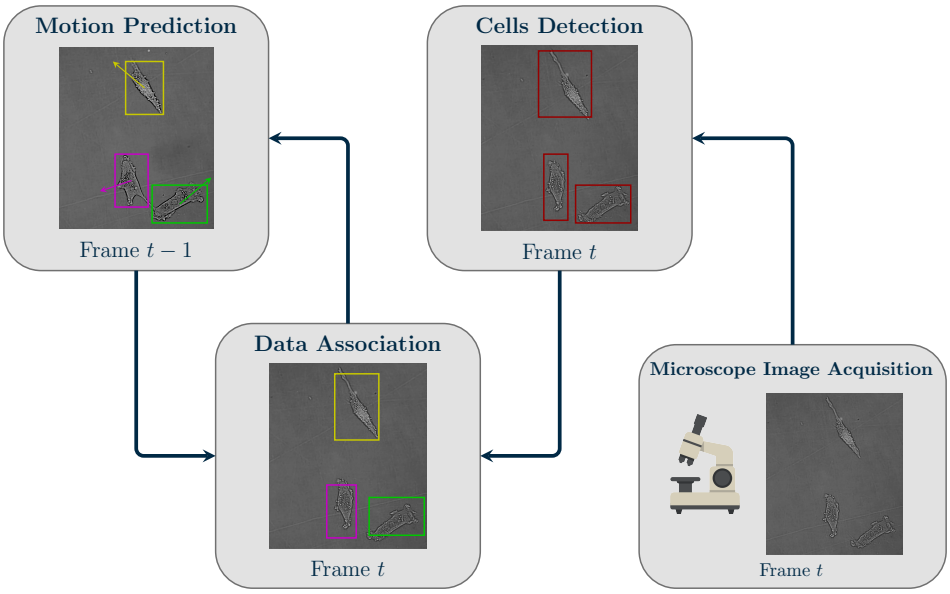

Figure 1: Scheme of a generic multi-cell tracking algorithm

localization of cells within images or video frames. Modern object detection methods often employ neural networks trained specifically for this task [35].

Motion prediction aims to estimate future positions of detected cells by combining their past trajectories with current detection measurements. This step is essential for ensuring track continuity and handling gaps or occlusions in the detections. Common techniques include Kalman filters, particle filters, and, most commonly, deep learning-based predictors. However, neural network predictors act as black boxes, thus limiting interpretability, and require large datasets, which are rare in this field. Instead, our approach models multi-cell behaviors explicitly and employs a closed-form solution for the identification of parameters, ensuring reliability and data efficiency.

Data association involves linking detected cells across consecutive frames to preserve their identities over time. This process requires matching detections from different frames and assigning them to the correct cell track. Motion models and similarity metrics are frequently used to assess the likelihood of accurate associations.

III. Heterogeneous Cell Populations as Open Multi-Agent Systems

In this section, we first formalize cell dynamics as an open multi-agent system. Then, we introduce a tailored class of parametric multi-agent terms to describe the interactions between heterogeneous cell populations within a general multi-culture scenario. These dynamical terms constitute the multi-agent model that will be then adopted in the proposed cell-tracking algorithm. The model design draws inspiration from a well-established line of research on bio-inspired multi-agent systems [29]. In particular, we extend to an open multi-agent framework neighboring terms motivated by swarm-like approaches, as in [36]

and [37], that describe both positional and morphological cell state behaviors. The latter terms are weighted by a set of parameters to be identified through data collected from time-lapse experiments.

A. Open Multi-Cell System Formalization

We model mitosis as an event where a parent cell splits into two new daughter cells. In this process, the parent cell is removed from the system and two new cells appear in its place. The latter cells retain the same type (i.e. agent type) as their parent. Moreover, to maintain distinct identities of cells over time, each cell is assigned a unique identifier label i. We consider a discrete-time framework, where $t \in \mathcal{T} \subseteq \mathbb{N}$ denotes the time index over an arbitrary horizon $\mathcal{T}$ (infinite or finite). In the context of a multi-culture experiment, we restrict attention to a finite time horizon, namely $\mathcal{T} = \{1, \dots, T\}$. Here, t will be the discrete-time variable representing the frame at which the system is observed, and with $T \in \mathbb{N} \setminus \{\infty\}$ denoting the final time instant at which the experiment concludes.

Additionally, we define the subset of time instants $\mathcal{T}_s \subset \mathcal{T}$ corresponding to switching times at which events related to cell population changes occur, i.e. when the number of cells within the observed frame changes, indicating a switch in the system dynamics. Moreover, we denote by $C^t_{\texttt{IN}} \in \mathbb{N}$ and $C^t_{\texttt{OUT}} \in \mathbb{N}$ the number of cells entering and exiting the heterogeneous cell population within the microscope FOV at time t, respectively. Let $L^t \subset \mathbb{N}$ be the set of labels identifying all the cells present in the scene at time t. Consequently, we introduce its subsets $L^t_p \subset L^t$ and $L^t_d \subset L^t \times L^t$ containing the labels of parent and daughter cells, respectively. Based on that, mitoses occurrences can be described through time-dependent sets of label pairs, identifying parent cells splitting into daughter cells at the current time. Formally, mitoses occurring at frame t are represented by

$$\mathcal{M}^t := \left\{ (i_p, \boldsymbol{j}_d) : i_p \in L^t_p \subset \mathbb{N}, \boldsymbol{j}_d \in L^t_d \subset \mathbb{N}^2 \right\}. \tag{1}$$

Instead, new cell entries into the camera field, at time t, are captured by the set $L^t_{\texttt{IN}} \subset \mathbb{N}$, such that

$$|\mathcal{M}^t| + |L^t_{\texttt{IN}}| = C^t_{\texttt{IN}}. \tag{2}$$

Similarly, cell exiting from the camera FOV at time t are described by the label set $L^t_{\texttt{OUT}} \subset \mathbb{N}$, verifying

$$|L^t_{\texttt{OUT}}| = C^t_{\texttt{OUT}}. \tag{3}$$

Note that $L^t_p \cap L^t_d \cap L^t_{\texttt{OUT}} \cap L^t_{\texttt{IN}} = \emptyset$, but for different time instants these sets may have non-null intersections. Moreover, at least one of these sets is non-empty at times $t \in \mathcal{T}_s$. The total number of cells at any time t, previously introduced as N^t, evolves according to

$$\begin{aligned} N^{t+1} &= N^t + C^t_{\texttt{IN}} - C^t_{\texttt{OUT}} \ \ \forall t \in \mathcal{T}_s \\ N^{t+1} &= N^t \ \ \forall t \notin \mathcal{T}_s. \end{aligned}$$

Moreover, the dynamics of the label set L^t can then be expressed as

$$L^{t+1} = \left(L^t \cup \bar{L}^t_d \cup L^t_{\texttt{IN}} \right) \setminus \left(L^t_p \cup L^t_{\texttt{OUT}} \right),$$

where $\bar{L}^t_d := \bigcup_{(a,b) \in L^t_d} \{a, b\}$ is the set of the individual elements from daughter cells label pairs.

Building upon the concepts introduced above, the following subsection presents the proposed open multi-agent parametric model.

B. Open Multi-Agent Parametric Model

We now introduce the open multi-cell system that models the cell dynamics for the tracking purpose. In this framework, each generic agent i represents a cell. The state of agent i at time t and its neighbor set are denoted by $\mathbf{x}^t_i \in \mathbb{R}^{n_x}$ and $\mathcal{N}^t_i \subset L^t$, respectively. To support a general multi-culture scenario in which different cell populations are interacting, we consider $\Gamma \in \mathbb{N}$ distinct agent types, each representing a different cell type. Thus, each cell type will be associated a parameter $\boldsymbol{\theta}_\gamma \in \mathbb{R}^{n_\theta}$, $\gamma \in \{1, \dots, \Gamma\}$. We denote

$$\boldsymbol{\theta} := [\boldsymbol{\theta}_1^\top, \dots, \boldsymbol{\theta}_\Gamma^\top]^\top \in \mathbb{R}^{n_\theta \Gamma}, \tag{4}$$

the stack of the parameter vectors for each cell type. The constant parameters $\boldsymbol{\theta}$ will be learned from experimental data.

Let $L := \bigcup_{t=1}^T L^t$ denote the set of all agent labels across time. Then, each agent $i \in L$ is associated with a parameter vector $\boldsymbol{\theta}_{\gamma_i} \in \mathbb{R}^{n_\theta}$, determined by its type $\gamma_i \in \{1, \dots, \Gamma\}$. Based on that, agent dynamics are modeled according to the discrete-time formulation

$$\mathbf{x}^{t+1}_i = \mathbf{x}^t_i + f_i \left(\mathbf{x}^t_i, \left\{ \mathbf{x}^t_j \right\}_{j \in \mathcal{N}^t_i}, \boldsymbol{\theta}_{\gamma_i}, t \right), \ \forall i \in L^{t+1} \cap L^t, \tag{5}$$

where the function f_i captures the dynamics of agent i based on its current state, the states of its neighboring agents, and its type-based parameters $\boldsymbol{\theta}_{\gamma_i}$. This formulation accounts for both cell state and type interactions, allowing the model to represent heterogeneous behaviors within a multi-culture experimental setting.

We propose coordinates of a Minimum Enclosing Rectangle (MER) as agent state within the proposed Multi-Cell Tracking (MCT) algorithm. This representation of cell morphology is defined as

$$\mathbf{x}_{MER,i} := \left[\mathbf{p}_i^\top, s_i, r_i, \phi_i, \mathbf{v}_i^\top, v_{s,i}, v_{r,i}, \omega_i\right]^\top, \tag{6}$$

where $\mathbf{p}_i, \mathbf{v}_i \in \mathbb{R}^2$ denote the center position and velocity of the cell, $s_i, r_i \in \mathbb{R}$ its area and aspect ratio, and $v_{s,i}, v_{r,i} \in \mathbb{R}$ their respective rates of change. The orientation angle $\phi_i \in [0, 2\pi]$ specifies the rotation of the MER relative to a fixed reference axis, and $\omega_i \in \mathbb{R}$ is the angular velocity. This state representation is especially suitable for tracking cells with fusiform or anisotropic morphologies, as it captures orientation and aspect more faithfully than the standard bounding box format. Moreover, it leads to more informative outputs at the end of the tracking pipeline, supporting better discrimination between different types based on shape dynamics. However, standard performance metrics for tracking algorithms are typically designed for axis-aligned bounding boxes. As a result, evaluating tracking accuracy on the state format in (6) requires custom metrics that are not always readily available or comparable with prior work. To facilitate benchmarking and compatibility with existing evaluation frameworks, our algorithm also supports a simplified state representation based on axis-aligned bounding boxes. Formally,

$$\mathbf{x}_{BB,i} := \left[\mathbf{p}_i^\top, s_i, r_i, \mathbf{v}_i^\top, v_{s,i}, v_{r,i}\right]^\top, \tag{7}$$

where the state variables retain the same semantics as in (6), but omit orientation and angular velocity. This compact version is especially useful for performance evaluation and comparison with other methods, while still capturing essential information about cell shape and motion.

Based on these two representations, the neighbors of cell i at time t in (5) can be defined as

$$\mathcal{N}_i^t := \left\{j \neq i : \left\|\mathbf{p}_i^t - \mathbf{p}_j^t\right\| \leq R_s,\ \{i,j\} \subseteq L^t\right\},$$

where R_s is a sensing radius that defines the region of space in which other cells are perceived. Here, we consider R_s as a priori fixed quantity (not learnable).

Building on the generic formulation of the open multi-agent model in (5), we now specify the individual terms governing the dynamics of each state component. For better readability, we first define subgroups of the whole state

$$\begin{aligned}
\boldsymbol{\pi}_i &:= [\mathbf{p}_i^{t\top}, \mathbf{v}_i^{t\top}]^\top \in \mathbb{R}^4 \\
\boldsymbol{\sigma}_i &:= [s_i^t, v_{s,i}^t]^\top \in \mathbb{R}^2 \\
\boldsymbol{\rho}_i &:= [r_i^t, v_{r,i}^t]^\top \in \mathbb{R}^2 \\
\boldsymbol{\eta}_i &:= [\phi_i^t, \omega_i^t]^\top \in \mathbb{R}^2.
\end{aligned}$$

Then, for the MER state format, the dynamics of cell i of type γ_i are given by

$$\mathbf{p}_i^{t+1} = \mathbf{p}_i^t + \mathbf{v}_i^t \tag{8a}$$
$$s_i^{t+1} = s_i^t + v_{s,i}^t \tag{8b}$$
$$r_i^{t+1} = r_i^t + v_{r,i}^t \tag{8c}$$
$$\phi_i^{t+1} = \phi_i^t + \omega_i^t \tag{8d}$$
$$\mathbf{v}_i^{t+1} = \mathbf{v}_i^t + f_{i,1}\left(\boldsymbol{\pi}_i, \{\boldsymbol{\pi}_j\}_{j\in\mathcal{N}_i^t}, \boldsymbol{\theta}_{\gamma_i}\right) \tag{8e}$$
$$v_{s,i}^{t+1} = v_{s,i}^t + f_{i,2}\left(\boldsymbol{\sigma}_i, \{\boldsymbol{\sigma}_j\}_{j\in\mathcal{N}_i^t-1}, \boldsymbol{\theta}_{\gamma_i}\right) \tag{8f}$$
$$v_{r,i}^{t+1} = v_{r,i}^t + f_{i,3}\left(\boldsymbol{\rho}_i, \{\boldsymbol{\rho}_j\}_{j\in\mathcal{N}_i^t}, \boldsymbol{\theta}_{\gamma_i}\right) \tag{8g}$$
$$\omega_i^{t+1} = \omega_i^t + f_{i,1}\left(\boldsymbol{\eta}_i, \{\boldsymbol{\eta}_j\}_{j\in\mathcal{N}_i^t}, \boldsymbol{\theta}_{\gamma_i}\right), \tag{8h}$$

where

$$f_{i,1} := \theta_{\gamma_i,1}\left(\frac{1}{|\mathcal{N}_i^t|}\sum_{j\in\mathcal{N}_i t}\mathbf{p}_j^t - \mathbf{p}_i^t\right) + \theta_{\gamma_i,2}\left(\frac{1}{|\mathcal{N}_i t|}\sum_{j\in\mathcal{N}_i t}\mathbf{v}_j^t - \mathbf{v}_i^t\right) + \theta_{\gamma_i,3}\sum_{j\in\mathcal{N}_i t}\frac{\mathbf{p}_i^t - \mathbf{p}_j^t}{\left\|\mathbf{p}_i^t - \mathbf{p}_j^t\right\|^2}, \tag{9}$$

captures the tendency to cohesion, alignment, and repulsion behaviors, while the shape-related terms

$$\begin{aligned}
f_{i,2} &:= \theta^\star_{\gamma_i,4}\left(S_{\gamma_i} - s_i^t\right) \\
f_{i,3} &:= \theta^\star_{\gamma_i,6}\left(R_{\gamma_i} - r_i\right),
\end{aligned} \tag{10}$$

model the tendency to maintain a certain target area $S_{\gamma_i} \in \mathbb{R}$ and target aspect ratio $R_{\gamma_i} \in \mathbb{R}$, considering cells of type γ_i. Finally, we note that for the standard bounding box state defined in (7), the dynamics can be fully described using only equations (8a)-(8c) and (8e)-(8g).

C. Identification of Model Parameters

We now present the proposed approach for identifying parameters within the multi-agent dynamics discussed in Section III-B. Here, we consider a generic formulation with Γ agent populations captured by parameters $\boldsymbol{\theta} \in \mathbb{R}^{n_\theta \Gamma}$, thus providing a flexible tool scalable to different experimental frameworks. Therefore, we propose an identification method tailored to open multi-cell systems, like those described in Section III-A.

The goal is to identify the parameters and obtain estimates that fit a training set of real cell trajectories extracted from *in vitro* co-culture experiments. Consider a dataset consisting of T image frames with the relative cell segmentations and tracks. From the latter, for each frame t we have access to $\mathbf{p}_i^t$, s_i^t, r_i^t and ϕ_i^t for all cells i. From these, we compute the relative velocities $\mathbf{v}_i^t$, $v_{s,i}^t$, $v_{r,i}^t$ and ω_i^t using differentiation methods. We tested various differentiation methods commonly used in system identification from time series data, such as finite differences, smoothed finite differences, Savitzky-Golay filtering, spline interpolation, and Kalman-based filtering, which are also discussed in the context of data-driven model identification (e.g., in [38]). In the experimental tests, we adopted a Kalman-based differentiation approach, which provided smoother estimates and led to smaller residuals in the subsequent model identification phase. This approach allows us to approximate the necessary time derivatives despite the intrinsic stochasticity and noise in biological cell dynamics and aligns with established practices in the literature.

Since we defined the dynamics in equation (5) as a weighted sum of multi-agent state terms, and imposed sensing radius R_s to be not learnable, we end up having a system with linear dependence in $\boldsymbol{\theta}$. Therefore, by properly redefining the system we can construct and solve a typical linear least squares (LLS) problem. The solution to the LLS problem is obtained by solving

$$\boldsymbol{\theta}^\star = \underset{\boldsymbol{\theta}}{\operatorname{argmin}} \ \|\mathbf{Y} - \mathbf{D}\boldsymbol{\theta}\|^2 , \tag{11}$$

where observation matrices are

$$\mathbf{Y}_i := [\mathbf{y}_i^1, \dots, \mathbf{y}_i^T]^\top \in \mathbb{R}^{n_x T}, \tag{12a}$$

$$\mathbf{Y} := [\mathbf{Y}_1^\top, \dots, \mathbf{Y}_N^\top]^\top \in \mathbb{R}^{n_x T N}. \tag{12b}$$

and design matrix

$$\mathbf{D} := [\mathbf{D}_1, \dots, \mathbf{D}_\Gamma] \in \mathbb{R}^{(n_x T N) \times \Gamma n_\theta},$$

in which each $\mathbf{D}_\gamma \in \mathbb{R}^{(n_x T N) \times n_\theta}$ represents the block corresponding to type γ agents. The latter are defined as

$$\mathbf{D}_\gamma := [\mathbf{D}_{\gamma,1}^\top, \dots \mathbf{D}_{\gamma,N}^\top]^\top \ \ \forall \gamma \in \{1, \dots, \Gamma\},$$

where $N := |L|$ is the total number of cells in the dataset, considered here as a single time-lapse experiment.

For all the cells $i \in L$, we specify the entries of the observation matrices (12a) as

$$\mathbf{y}_i^t = \begin{cases} \left[\mathbf{x}_i^t - \mathbf{x}_i^{t-1}\right]^\top & \text{if } \ i \in L^t \cap L^{t-1} \\ \mathbf{0}_{n_x}^\top & \text{otherwise} \end{cases} .$$

Instead, the single-cell design matrices are constructed as

$$\mathbf{D}_{\gamma,i} = \begin{bmatrix} d_{i,1}^1 & d_{i,2}^1 & \dots & d_{i,n_\theta}^1 \\ \vdots & \vdots & & \vdots \\ d_{i,1}^T & d_{i,2}^T & \dots & d_{i,n_\theta}^T \end{bmatrix} = \begin{bmatrix} \boldsymbol{d}_i^1 \\ \vdots \\ \boldsymbol{d}_i^T \end{bmatrix} \in \mathbb{R}^{n_x T \times n_\theta},$$

verifying that for each t

$$\boldsymbol{d}_i^t = \mathbf{0}_{n_x \times n_\theta} \ \ \forall \gamma \neq \gamma_i \text{ or } i \notin L^t.$$

This condition, adding sparsity to the design matrix, ensures feasibility by limiting the data to cells present at the current frame t and by selecting different weights based on type γ_i. Otherwise, the entries of cell $i \in L^t$ are functions of the considered cell and its neighbor states

$$\begin{aligned} d_{i,1}^t &= f_{i,1}\left(\mathbf{x}_i^t, \{\mathbf{x}_j^t\}_{j \in \mathcal{N}_i^t}\right) \\ &\vdots \\ d_{i,n_\theta}^t &= f_{i,n_\theta}\left(\mathbf{x}_i^t, \{\mathbf{x}_j^t\}_{j \in \mathcal{N}_i^t}\right). \end{aligned} \tag{13}$$

Note that, since $n_x T N \gg \Gamma n_\theta$ then $\left(\mathbf{D}^\top \mathbf{D}\right)^{-1}$ exists if and only if $\operatorname{rank}(\mathbf{D}) = \Gamma n_\theta$. The only case where this condition is not met is when, for an instant of time $t \in \{1, \dots, T\}$, there are no agents present in the scene, meaning that $L^t = \emptyset$. However, in our framework, we can assume that $L^t \neq \emptyset \ \forall t$ since we work with videos in which at least one cell is always

present throughout the entire duration of the experiment. The solution of (11) that best fits cell trajectories extracted from a single experiment is

$$\boldsymbol{\theta}^{\star} = \left(\mathbf{D}^{\top}\mathbf{D}\right)^{-1}\mathbf{D}^{\top}\mathbf{Y}. \tag{14}$$

In the case of multi-experiment data, such as in our scenario, the process involves stacking observation vectors and design matrices for each data collection. Moreover, considering the scarcity of data in biological cell experiments, transformed versions of the same data sequences can be included to enhance robustness concerning invariance transformations, such as rotations, and horizontal and vertical flips. Details on the augmentation of the dataset are given in Section V on numerical experiments.

IV. Multi Cell Tracking Algorithm

In this section, we detail our solution to the cell-tracking problem outlined in Section II. Our Heterogeneous Open Multi-Cell EKF-based Tracking (HEOM-EKF) algorithm introduces a novel motion prediction step employing a tailored Extended Kalman Filter for Open Multi-Agent systems that leverages the models described in Section III. Moreover, our algorithm includes a procedure to estimate cell population changes and reconstruct the cell lineage tree. The main steps of the algorithm are detailed in Algorithm 1.

Algorithm 1 HEOM-EKF

Initialization
  Obtain $\mathbf{Z}^0$ from detector
  Initialize EKF: $\hat{\mathbf{X}}^{0|0} = \mathbf{Z}^0$, $\mathbf{P}^{0|0}$, $\mathbf{Q}^0$, $\mathbf{R}^0$ and $\mathbf{H}^0$
  Initialize mitosis set: $\hat{\mathcal{M}}^t = \emptyset \; \forall t \in \mathcal{T}$
for each frame $t \in \mathcal{T}$ **do**
  Object Detection:
    Obtain $\mathbf{Z}^t$ from detector
  EKF Prediction Step:

$$\hat{\mathbf{X}}^{t|t-1} = \hat{\mathbf{X}}^{t-1|t-1} + f\left(\hat{\mathbf{X}}^{t-1|t-1}, \boldsymbol{\theta}^{\star}\right) \tag{15}$$

$$\mathbf{F}^{t-1} = \frac{\partial f}{\partial \mathbf{X}}\Big|_{\hat{\mathbf{X}}^{t-1|t-1}} \tag{16}$$

$$\mathbf{P}^{t|t-1} = \mathbf{F}^{t-1}\mathbf{P}^{t-1|t-1}\left(\mathbf{F}^{t-1}\right)^{T} + \mathbf{Q}^t \tag{17}$$

  Associate Detections to Predictions:
    Get $\mathbf{S}^t$ via (25) and $\mathbf{A}^t$ solving (26)
    Reorder detections IDs in $\mathbf{Z}^t$ based on $\mathbf{A}^t$
  EKF Update Step:

$$\mathbf{K}^t = \mathbf{P}^{t|t-1}\mathbf{H}^{t\top}(\mathbf{H}^t\mathbf{P}^{t|t-1}\mathbf{H}^{t\top} + \mathbf{R}^t)^{-1} \tag{18}$$

$$\hat{\mathbf{X}}^{t|t} = \hat{\mathbf{X}}^{t|t-1} + \mathbf{K}^t(\mathbf{Z}^t - \mathbf{H}^t\hat{\mathbf{X}}^{t|t-1}) \tag{19}$$

$$\mathbf{P}^{t|t} = (\mathbf{I} - \mathbf{K}^t\mathbf{H}^t)\mathbf{P}^{t|t-1} \tag{20}$$

  Search for Population Change Event:
    $\hat{\mathcal{M}}^t, \hat{L}_p^t, \hat{L}_d^t = \textsc{mitosis-detect}(\mathbf{Z}^t, \hat{\mathbf{X}}^{t|t}, \mathbf{S}^t, d_{\max}, IoU_{\min})$
    $\hat{L}_{\mathtt{IN}}^t, \hat{L}_{\mathtt{OUT}}^t = \textsc{in-out-detect}(\mathbf{Z}^t, \hat{\mathbf{X}}^{t|t}, \mathbf{S}^t, t_{\max}, d_{\max}, IoU_{\min}, \epsilon)$
  if $\hat{L}_p^t \cup \hat{L}_d^t \cup \hat{L}_{\mathtt{OUT}}^t \cup \hat{L}_{\mathtt{IN}}^t \neq \emptyset$ **then**
    $\hat{\mathcal{T}}_s \cup \{t\}$
    Update $\hat{\mathbf{X}}^{t|t}$, $\mathbf{P}^{t|t}$, $\mathbf{Q}^t$, $\mathbf{R}^t$ and $\mathbf{H}^t$ via Algorithm 4
  end if
end for
return Cell tracks $\hat{\mathbf{X}}^{t|t} \; \forall t$ and cell lineage tree $\hat{\mathcal{M}}^t \; \forall t$

Here, the set estimations $\hat{L}_p^t$, $\hat{L}_d^t$, $\hat{L}_{\mathtt{OUT}}^t$, $\hat{L}_{\mathtt{IN}}^t$ and $\hat{\mathcal{M}}^t$ refer to the previous definitions of true quantities introduced in Section III defined in (1)-(3). We also provide a graphical illustration (see Figure 2) of how HEOM-EKF behaves in the presence of a mitosis event and how these label set estimates change accordingly across frames.

In particular, the algorithm starts by initializing the state guess with detections at the first frame and setting up the EKF matrices. Then, throughout each frame, the algorithm iterates through three main steps. First, get the cell detections related to

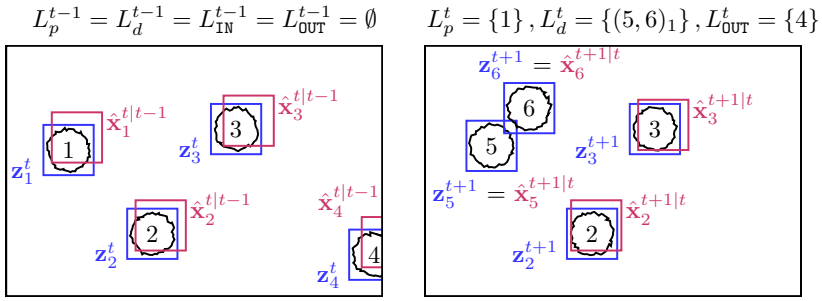

Figure 2: An illustrative example of label sets at different frames in a tracking scenario.

the current image. Second, it predicts the next state via the EKF prediction step leveraging the interaction dynamics learned from real data, whose identification of parameters is described in Section III-C. Third, it associates detections to predictions and updates the state estimate through the so-called EKF update step. Differently from standard filtering schemes, this step takes also into account for changing in the number of cells. Specifically, when a cell population change is predicted at current frame, through MITOSIS-DETECT and IN-OUT-DETECT procedures (see Algorithms 2-3), the EKF update variables are adapted to account for dimensionality variations (see Algorithm 4). We now detail all the steps in the algorithm.

A. Object Detection

The object detection phase serves as the initial step in our algorithm, with the primary goal of localizing cells in consecutive frames of the input video. All quantities and computations in our algorithm are directly based on the pixel coordinates of the detected cells. This ensures consistency with the spatial information provided during the object detection step. In particular, the measurement of cell i obtained via object detection at frame t is an oriented bounding box. Formally

$$\mathbf{z}_i := \left[\mathbf{p}_i^\top, s_i, r_i, \phi_i\right]^\top. \tag{21}$$

Here, $\mathbf{p}_i$ denotes the center coordinates of the bounding box for the ith cell. The terms $s_i, r_i \in \mathbb{R}$ represent the area and aspect ratio of the detected region, respectively, while $\phi_i \in [0, 2\pi]$ indicates the orientation angle.

It is worth noting that the object detection is performed independently on each frame, producing frame-specific cell detections and measurements, denoted as $\mathbf{z}_i^t$. The identity labels i are assigned arbitrarily by the detector, regardless of the method used. To ensure consistent tracking across frames prediction and data association steps (see Sections IV-C and IV-B) are needed to reorder and match cell identities over time.

B. Motion Prediction

At each time t, the object detection phase yields a collection of measurement vectors $\mathbf{z}_i^t \in \mathbb{R}^{n_z}$ (cf. Section IV-A). Based on that, we can now detail the motion prediction step.

Let $\mathbf{x}_i^t \in \mathbb{R}^{n_x}$ denote the true, unknown state of cell i at time t, represented in the format of equation (6). Accordingly, the detection process at each frame t can be modeled by the following measurement equation

$$\mathbf{z}_i^t = \mathbf{I}_{n_z \times n_x} \mathbf{x}_i^t + \mathbf{w}_z, \qquad \forall\, i \in L^t, \tag{22}$$

in which $\mathbf{I}_{n_z \times n_x}$ is the observation matrix, which is assumed to be constant and identical across all measurements. The term $\mathbf{w}_z \in \mathbb{R}^{n_z}$ denotes zero-mean Gaussian noise with covariance $\mathbf{R}^t$.

Let us introduce $\hat{\mathbf{x}}_i^{t|t-1} \in \mathbb{R}^{n_x}$ as the predicted state of ith cell at time t, obtained after a prediction step in which the measurement $\mathbf{z}^{t-1}$ is known. Instead, $\hat{\mathbf{x}}_i^{t|t} \in \mathbb{R}^{n_x}$ represents the updated estimate through the measurement $\mathbf{z}_i^t$ obtained after an estimation update step. To retrieve the aforementioned predictions, our tracking algorithm adopts an Extended Kalman Filter [39] incorporating as nonlinear dynamics the open multi-agent model introduced in Subsection III-B.

We first define

$$\mathbf{X}^t := [\mathbf{x}_1^{t\,\top}, \ldots, \mathbf{x}_{N^t}^{t\,\top}]^\top \in \mathbb{R}^{N^t n_x}$$
$$\mathbf{Z}^t := [\mathbf{z}_1^{t\,\top}, \ldots, \mathbf{z}_{N^t}^{t\,\top}]^\top \in \mathbb{R}^{N^t n_z},$$

as the stack of cell population states and measurements. Similarly, we denote by $\hat{\mathbf{X}}^{t|t-1}$ and $\hat{\mathbf{X}}^{t|t}$ the stacks of predicted and updated state estimates, respectively. According to expression (22), the stack measurement vector is given by

$$\mathbf{Z}^t = \mathbf{H}^t \mathbf{X}^t + \mathbf{W}_z^t, \tag{23}$$

where $\mathbf{H}^t \in \mathbb{R}^{(N^t n_z)\times(N^t n_x)}$ and $\mathbf{W}_z^t \in \mathbb{R}^{N^t n_z}$ are the stacks $\forall i \in L^t$ of observation matrices and measurement noise vectors, respectively.

The multi-agent dynamics used to predict the ith cell state belong to the class of models introduced in Section III-B, i.e.

$$\hat{\mathbf{X}}^{t|t-1} = \hat{\mathbf{X}}^{t-1|t-1} + f\left(\hat{\mathbf{X}}^{t-1|t-1}, \boldsymbol{\theta}^\star, t\right) + \mathbf{W}_x^t,$$

which is the predicted version of equation (5) written in compact form. In particular, $f : \mathbb{R}^{n_x N^t} \times \mathbb{R}^{n_\theta \Gamma} \times \mathbb{R} \mapsto \mathbb{R}^{n_x N^t}$ suitably stacks the dynamics in (8) for all the agents present at current time, and $\mathbf{W}_x^t \in \mathbb{R}^{n_x N^t}$ stacks the noise vector $\mathbf{w}_x$ for all the cells. The noise $\mathbf{w}_x \in \mathbb{R}^{n_x}$ is a Gaussian random variable with zero mean and covariance $\mathbf{Q}$. The optimal parameters in (15) are learned by solving (14) with properly constructed $\mathbf{D}$ and $\mathbf{Y}$ (see Section III-C) on real data. The step in (17) is the update of the so-called estimation error covariance matrix $\mathbf{P}^t \in \mathbb{R}^{n_x N^t \times n_x N^t}$. The steps in (18)–(20) instead perform the update steps of the EKF. Here, $\mathbf{K}^t \in \mathbb{R}^{n_x N^t \times n_z N^t}$ is the Kalman gain matrix.

Thanks to this motion prediction design, our tracker can operate on a unified state representation for the heterogeneous cell populations taking advantage of the sparse structure of the dynamics. Indeed, the motion prediction of each cell is performed considering interactions between neighboring cells rather than independent dynamical entities.

C. Data Association

The data association step bridges the gap between detected cells across consecutive frames, preserving their identities over time. Indeed, given two consecutive time frames $t-1$ and t, the ith cell may be detected and associated with different labels. At the generic time t, the EKF predictions in (15) provide the estimate of a novel bounding box $\hat{B}_i$ for cell i. This predicted box is centered in $\hat{\mathbf{p}}_i^{t|t-1}$ and has area and aspect ratio $\hat{s}_i^{t|t-1}$ and $\hat{r}_i^{t|t-1}$, respectively. Considering the cell state as in (6), also the predicted box orientation $\hat{\phi}_i^{t|t-1}$ is present.

Similarly, let B_j denote the jth bounding box found by the detection step. Let us introduce the similarity matrix $\mathbf{S}^t \in \mathbb{R}^{N^t \times N^t}$ at image frame t, with single entry

$$\left[\mathbf{S}^t\right]_{ij} = \mathcal{S}\left(\hat{B}_i, B_j\right), \tag{24}$$

where $\mathcal{S}$ is a similarity function computed between the predicted bounding box of ith cell and the detected one of jth cell at time t. In this work, we use the so-called Intersection Over Union (IoU) metric [40], so that

$$\left[\mathbf{S}^t\right]_{ij} = \frac{|\hat{B}_i \cap B_j|}{|\hat{B}_i \cup B_j|}. \tag{25}$$

Given $\mathbf{S}^t$, the data association problem regards finding an optimal assignment matrix $\mathbf{A}^t$ at each frame of the video that maximizes the total similarity across all associations. This means solving at each time t the following linear-assignment problem

$$\begin{aligned} &\max \sum_{i,j} \left[\mathbf{S}^t\right]_{ij} a_{ij} \\ &\text{s.t.} \ \sum_j a_{ij} = 1 \ \forall i, \ \ \sum_i a_{ij} = 1 \ \forall j, \ \ a_{ij} \in \{0,1\}, \end{aligned} \tag{26}$$

where each entry $a_{ij} = 1$ in $\mathbf{A}^t$ indicates that j^{th} detection is assigned to i^{th} prediction, and $a_{ij} = 0$ otherwise. This problem can be solved in polynomial time leveraging, e.g., the Hungarian algorithm [41]. To reject associations with a poor similarity index, we enforced a threshold for the IoU function in (25), denoted as $IoU_{\min}$.

We now define the set $\mathcal{U}$ containing unmatched elements at time t, which can be further divided into unmatched predictions $\mathcal{U}_{\hat{x}}^t$ and unmatched detections $\mathcal{U}_z^t$. Specifically, the set of unmatches is defined as

$$\mathcal{U}^t := \left\{(i,j) : \left[\mathbf{S}^t\right]_{ij} \leq IoU_{\min}\right\}.$$

Then, we derive the subsets for unmatched predictions and unmatched detections

$$\mathcal{U}_{\hat{x}}^t := \bigcup_{(i,j)\in\mathcal{U}^t} \{i\}, \ \ \mathcal{U}_z^t := \bigcup_{(i,j)\in\mathcal{U}^t} \{j\}. \tag{27}$$

To provide better context, unmatched predictions and detections arise within a tracking algorithm where associations between predicted states and detections may not always be successful. In such cases, elements that fail to match are categorized into these sets to facilitate further analysis or handling in the tracking process.

D. Cell Population Changes and Cell Lineage Tree

In this subsection, we define three routines used in our cell tracking strategy HEOM-EKF. We first introduce a method for estimating cell mitosis events (Algorithm 2). Then, we describe how to detect the entry and exit of cells within the microscope FOV (Algorithm 3). Lastly, we present the procedure to update the dimensions of the EKF matrices in response to the changes in the cell population (Algorithm 4).

We begin by introducing some quantities used within Algorithm 2 and 3. Let $N_z^t \in \mathbb{N}$ be the number of detected cells and $N_{\hat{x}}^t \in \mathbb{N}$ the number of predicted cell states. Also, let $\bar{\mathcal{U}}^t \subset \mathcal{U}^t$ be the subset of unmatched predicted and detected cells whose bounding boxes have no intersection and whose distance exceeds the mitosis threshold $d_{\max}$. This distance is determined based on real observed behaviors within the co-culture experiments, and it represents the maximum center distance at which a mitosis event is usually detected. Formally,

$$N_z^t := \frac{\dim\left(\mathbf{Z}^t\right)}{n_z}, \quad N_{\hat{x}}^t := \frac{\dim\left(\hat{\mathbf{X}}^{t|t-1}\right)}{n_x} \tag{28}$$

$$\bar{\mathcal{U}}^t := \left\{(i,j) \in \mathcal{U}^t : \left[\mathbf{S}^t\right]_{ij} = 0, \left\|\hat{\mathbf{p}}_i^t - \mathbf{p}_j^t\right\| \geq d_{\max}\right\} \tag{29}$$

$$\bar{\mathcal{U}}_{\hat{x}}^t := \bigcup_{(i,j)\in\bar{\mathcal{U}}_{\hat{x}}^t} \{i\}, \quad \bar{\mathcal{U}}_z^t := \bigcup_{(i,j)\in\bar{\mathcal{U}}_z^t} \{j\}. \tag{30}$$

The ability to accurately determine mitosis events is important for extracting relevant information about the evolution of heterogeneous cell populations over time. A possible approach consists of constructing the cell lineage tree for each cell. To this end, in the following, we present Algorithm 2.

Algorithm 2 MITOSIS-DETECT : Get set estimate $\hat{\mathcal{M}}^t$

Require: $\mathbf{Z}^t$, $\hat{\mathbf{X}}^{t|t}$, $\mathbf{S}^t$, $d_{\max}$, $IoU_{\min}$

if $\mathcal{U}_z^t \neq \emptyset$ **and** $N_z^t > \left(N_{\hat{x}}^t - |\mathcal{U}_{\hat{x}}^t| + |\bar{\mathcal{U}}_{\hat{x}}^t|\right)$ **then**

  for $i \in \mathcal{U}_z^t \setminus \bar{\mathcal{U}}_z^t$ **do**

    Find $j = \underset{j}{\operatorname{argmin}} \left\|\mathbf{z}_i^t - \mathbf{z}_j^t\right\|$

    New prediction labels: from (i,j) to (j_{d_1}, j_{d_2})

    Update daughters set $\hat{L}_d^t = \hat{L}_d^{t-1} \cup \{j_{d_1}, j_{d_2}\}$

    Update parent set $\hat{L}_p^t = \hat{L}_p^{t-1} \cup \{j\}$

  end for

end if

Update $\hat{\mathcal{M}}^t$ based on definition (1)

return $\hat{\mathcal{M}}^t$, $\hat{L}_p^t$, $\hat{L}_d^t$

The proposed method estimates mitosis occurrences at a given frame t by computing the set estimates $\hat{L}_p^t$, $\hat{L}_d^t$, and thus $\hat{\mathcal{M}}^t$. In particular, the algorithm leverages the sets in (27) and (30), together with the quantities in (28), to distinguish new detections due to mitosis, cells entering the camera FOV or unmatched detections. After tracking is completed across the entire video sequence, the lineage of each cell is constructed using the parent-child relationships stored in the sets $\hat{\mathcal{M}}^t$ for all $t \in \mathcal{T}$. Note that $\hat{\mathcal{M}}^t = \emptyset$ at frames where no mitosis events are detected.

We now present Algorithm 3 to estimate the occurrence of cells entering or exiting from the camera FOV.

Analogously to Algorithm 2, this method begins by checking for unmatched detections at the current frame t, using the sets defined in (27) and (30), along with the values in (28). It then examines the set $\bar{\mathcal{U}}_z^t$ to identify detected cells that are ϵ-close to the image boundaries $(\bar{x}, \bar{y})$, i.e., cells that have recently entered the field of view. To detect cells that are leaving the microscope FOV, the algorithm instead looks for predictions that remained unmatched over the past $t_{\max}$ time steps. If these predictions are also ϵ-close to the image boundaries, they are considered as outcoming cells.

Algorithm 4 takes care of adapting the dimensions of EKF matrices. Specifically, it reorganizes the terms $\hat{\mathbf{X}}^{t|t-1}$, $\hat{\mathbf{P}}^{t|t-1}$, $\mathbf{H}^t$, $\mathbf{R}^t$, and $\mathbf{Q}^t$ to ensure feasible tracking. Especially, let us define the functions used for including new daughter cells into the tracking procedure as

$$g_d\left(\boldsymbol{a}, \boldsymbol{b}\right) := \begin{bmatrix} \boldsymbol{a} \\ \boldsymbol{b} \end{bmatrix} \in \mathbb{R}^{(N+1)n_x},$$

in which $\boldsymbol{a} \in \mathbb{R}^{Nn_x}, \boldsymbol{b} \in \mathbb{R}^{n_x}$. Also, let

$$G_d\left(\boldsymbol{A}, \boldsymbol{b}\right) := \begin{bmatrix} \boldsymbol{A} & \boldsymbol{b}_{1:n_x-1} \\ \boldsymbol{b}_{1:n_x-1}^\top & b \end{bmatrix} \in \mathbb{R}^{(N+1)n_x \times (N+1)n_x},$$

Algorithm 3 IN-OUT-DETECT : Get set estimates $\hat{L}^t_{\texttt{IN}}$, $\hat{L}^t_{\texttt{OUT}}$

Require: $\mathbf{Z}^t$, $\hat{\mathbf{X}}^{t|t}$, $\mathbf{S}^t$, $t_{\max}$, $d_{\max}$, $IoU_{\min}$, ϵ

if $\mathcal{U}^t_z \neq \emptyset$ **and** $N^t_z > \left(N^t_{\hat{x}} - |\mathcal{U}^t_{\hat{x}}| + |\bar{\mathcal{U}}^t_{\hat{x}}|\right)$ **then**

for $i \in \bar{\mathcal{U}}^t_z : \min(p^t_{x,i}, \bar{x} - p^t_{x,i}, p^t_{y,i}, \bar{y} - p^t_{y,i}) \leq \epsilon$ **do**

New prediction label $i \rightarrow j_{\texttt{IN}}$

Update entry set $\hat{L}^t_{\texttt{IN}} = \hat{L}^{t-1}_{\texttt{IN}} \cup \{j_{\texttt{IN}}\}$

end for

end if

for $i \in \left\{\mathcal{U}^{t-t_{\max}}_{\hat{x}} \cap \ldots \cap \mathcal{U}^t_{\hat{x}}\right\}$ **do**

if $\min(p^t_{x,i}, \bar{x} - p^t_{x,i}, p^t_{y,i}, \bar{y} - p^t_{y,i}) \leq \epsilon$ **then**

Remove prediction label i

Update exit set $\hat{L}^t_{\texttt{OUT}} = \hat{L}^{t-1}_{\texttt{OUT}} \cup \{i\}$

end if

end for

return $\hat{L}^t_{\texttt{IN}}$, $\hat{L}^t_{\texttt{OUT}}$

in which $\boldsymbol{A} \in \mathbb{R}^{Nn_x \times Nn_x}$, $\boldsymbol{b} \in \mathbb{R}^{n_x}$, $\boldsymbol{b}_{1:n_x-1} \in \mathbb{R}^{n_x-1}$ and $b \in \mathbb{R}$. Instead, the functions used to remove a parent cell within HEOM-EKF are

$$\begin{aligned} g_p : \mathbb{R}^{Nn_x} \times \mathbb{R}^{n_x} &\rightarrow \mathbb{R}^{(N-1)n_x} \\ (\boldsymbol{a}, \boldsymbol{a}_i) &\mapsto [\boldsymbol{a}_1^\top, \ldots, \boldsymbol{a}_{i-1}^\top, \boldsymbol{a}_{i+1}^\top, \ldots, \boldsymbol{a}_N^\top]^\top, \end{aligned}$$

in which $\boldsymbol{a}_i$ belongs to $\boldsymbol{a} = [\boldsymbol{a}_1^\top, \ldots, \boldsymbol{a}_N^\top]^\top$, and

$$\begin{aligned} G_p : \mathbb{R}^{Nn_x \times Nn_x} \times \{1, \ldots, N\} &\rightarrow \mathbb{R}^{(N-1)n_x \times (N-1)n_x} \\ (\boldsymbol{A}, i) &\mapsto \boldsymbol{A}_{\setminus i}, \end{aligned}$$

with $\boldsymbol{A}_{\setminus i}$ being the matrix $\boldsymbol{A}$ with the ith row and column removed.

Algorithm 4 Update EKF dimensionality

Require: $\hat{L}^t_p$, $\hat{L}^t_d$, $\hat{L}^t_{\texttt{OUT}}$, $\hat{L}^t_{\texttt{IN}}$, $\hat{\mathbf{X}}^{t|t}$, $\mathbf{P}^{t|t}$, $\mathbf{Q}^t$, $\mathbf{R}^t$ and $\mathbf{H}^t$

for $i_p \in \hat{L}^t_p$ and $\boldsymbol{j}_d \in \hat{L}^t_d$ **do**

$\hat{\mathbf{X}}^{t|t} = g_p\left(\hat{\mathbf{X}}^{t|t}, \hat{\mathbf{x}}^{t|t}_{i_p}\right)$

$\hat{\mathbf{X}}^{t|t} = g_d\left(\hat{\mathbf{X}}^{t|t}, \mathbf{z}^t_j\right) \ \forall j \in \boldsymbol{j}_d$

$\mathbf{P}^{t|t} = G_p\left(\mathbf{P}^{t|t}, i_p\right)$

$\mathbf{P}^{t|t} = G_d\left(\mathbf{P}^{t|t}, [\mathbf{0}^\top_{n_x-1}, 1]^\top\right) \ \forall j \in \boldsymbol{j}_d$

end for

for $i_{\texttt{OUT}} \in \hat{L}^t_{\texttt{OUT}}$ **do**

$\hat{\mathbf{X}}^{t|t} = g_p\left(\hat{\mathbf{X}}^{t|t}, \hat{\mathbf{x}}^{t|t}_{i_{\texttt{OUT}}}\right)$

$\mathbf{P}^{t|t} = G_p\left(\mathbf{P}^{t|t}, i_{\texttt{OUT}}\right)$

end for

for $i_{\texttt{IN}} \in \hat{L}^t_{\texttt{IN}}$ **do**

$\hat{\mathbf{X}}^{t|t} = g_d\left(\hat{\mathbf{X}}^{t|t}, \mathbf{z}^t_{i_{\texttt{IN}}}\right)$

$\mathbf{P}^{t|t} = G_d\left(\mathbf{P}^{t|t}, [\mathbf{0}^\top_{n_x-1}, 1]^\top\right)$

end for

Redefine $\mathbf{Q}^t$, $\mathbf{R}^t$ and $\mathbf{H}^t$ according to N^t_z and $N^t_{\hat{x}}$

V. Numerical Experiments

In this section, we first introduce the dataset used in our simulations. Then, we present the results of the proposed cell-tracking algorithm, analyze the optimal multi-agent model parameters that confirm cell type discrimination, and discuss the extracted cell lineage tree.

A. Dataset

The dataset used in this study was derived from raw time-lapse image sequences captured using a confocal microscope (A1R MP microscope, Nikon) at IRCCS Istituto Ortopedico Rizzoli. The human 143b line were obtained from the American Type Cell Culture Collection (ATCC) and were cultured in Minimum Essential Medium Eagle Alpha modification (Sigma) with 10% fetal bovine serum (FBS, Sigma) and 1% penicillin/streptomycin (P/S) (Euroclone) and used for co-culture esperiments after trypsinization and semi-confluence. Human adipose-derived MSC (ATCC) were maintained in complete alpha-MEM with 10% fetal bovine serum (FBS, Sigma) and 1% P/S and used for co-culture esperiments after trypsinization and semi-confluence. Cells were incubated at 37 °C in 5% CO_2. GFP-transfected MSC cells, obtained as previously described [32], were used in co-culture experiments. For co-cultures, 143b cells and GFP+ MSC were mixed 1:3 and seeded in at low density in complete alpha-MEM in petri dishes for time-lapse imaging. The transfection with GFP allowed us to clearly distinguish MSC from 143b cells and, consequently, accurately assign the measured features between the two cell types. The set of experiments carried out consists of 4 videos with 172 frames each with images captured every 4 minutes (25x immersion objective, NA 1.1, RI 1.333).

Initial processing of the raw images was performed by using NIS Elements AR 5.40.01 software (Nikon), employed on all the images to perform semantic segmentation, labeling, and classification by cell type. We performed these tasks by combining manual adjustments with automated image processing tools. The primary objective of this step was to extract accurate data for training and testing the proposed tracking algorithm. Since the process could be subject to human and/or software automation errors, we refer to these annotations as the gold standard, rather than the actual ground truths. Following segmentation, the software extracted around 70 features per segmented object, including morphological and positional properties, allowing for detailed temporal analysis of each cell. These features, after filtering only the ones relevant to our purposes, provided a comprehensive characterization of the cells' dynamics and their interactions over time. To refine the dataset further, additional image processing techniques were applied, leveraging the Python package OpenCV [42], focusing on denoising and fixing any labeling or segmentation errors. The latter post-processing corrections ensured enhanced quality and reliability of the data.

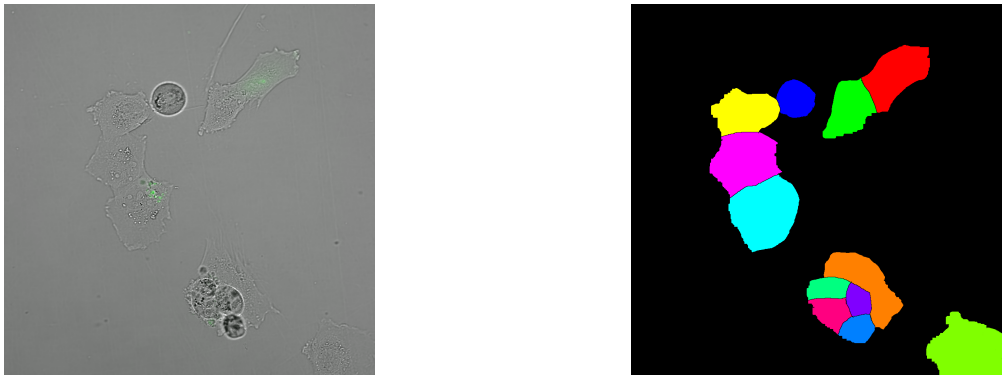

(a) (b)

Figure 3: Comparison between the original microscope image (a) and its final segmented version (b).

Before presenting the final result and tests, we first provide key statistics extracted from the dataset. Specifically, we selected relevant cell features that influenced the design of the open multi-agent dynamics. In Figure 4, we illustrate the mean and relative variance of shape-discriminating factors between MSC and 143b cells in one of the analyzed video sequences. Notably, MSC exhibit a more elongated, fibroblast-like shape, whereas osteosarcoma cells tend to be more rounded (higher circularity). Moreover, as an average, MSC are larger than 143b cells in terms of both area and perimeter.

Finally, we want to highlight that this dataset is a unique resource to study cellular behavior in co-culture frameworks, setting it apart from most publicly available datasets, such as the ones from the Cell Tracking Challenge, which only focus on monoculture experiments.

B. Cell Detection in Video Frames

In our experiments, we adopt a semi-automatic approach using the proprietary image-analysis software included with our microscope. This choice offers several advantages: (i) it simplifies the detection pipeline, allowing us to focus on assessing the performance of our novel motion prediction module; (ii) it avoids the need for large, annotated datasets typically required for supervised training; and (iii) it ensures compatibility and consistency with the data acquisition process, as the detection tool is tailored to the imaging system. For each video frame, the software provides region proposals (cell segmentations), from which axis-aligned or oriented bounding boxes can be extracted using basic image processing techniques. State-of-the-art cell segmentation tools rely on training and deploying a dedicated deep learning model for cell detection, as in [43], [44]. However, these approaches typically require a large amount of data and do not discriminate between different cell populations. Our

multi-agent approach to cell tracking aims to introduce dynamical system knowledge into the process. This improves tracking performance even when the object detection component cannot exploit a large amount of data.

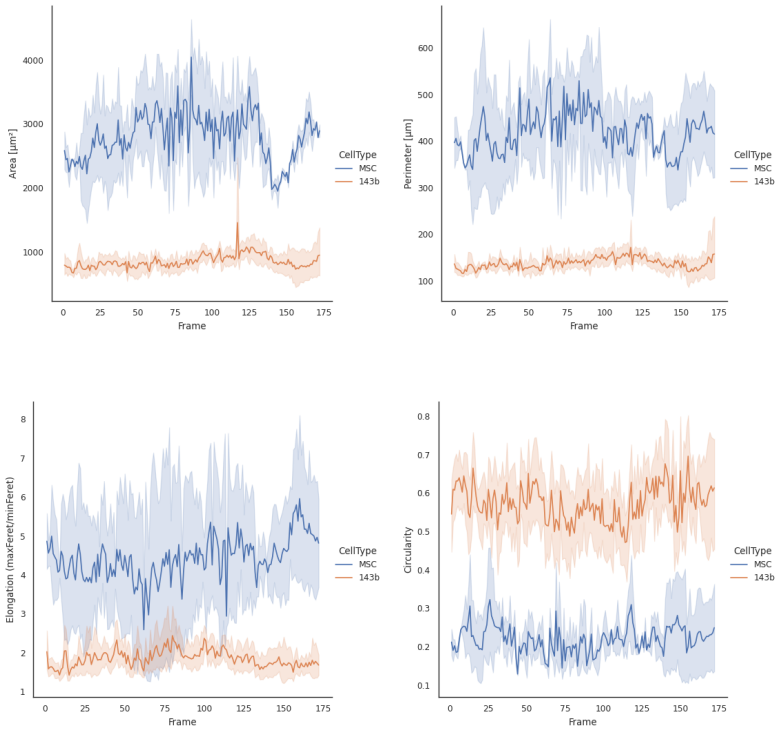

Figure 4: Mean and variance over time for the area, outer perimeter, circularity, and elongation, categorized by cell type. Shown as an example from one experiment to illustrate cell type discrimination.

C. Experimental Results

We implemented the proposed methodology via the Python 3 programming language, testing our MCT algorithm on co-culture videos from *in vitro* experiments involving MSC and osteosarcoma cells.

Given the limited dataset of only four videos, we employed a cross-validation approach [45]. Specifically, we trained the models described in Section III, by computing the optimal solution $\boldsymbol{\theta}^*$ as in (11) considering three videos regarding a co-culture scenario ($\Gamma = 2$). Then we evaluated the tracking performances on the remaining one. We repeated this procedure for all possible combinations of training and test videos.

To improve the robustness of our estimation and mitigate overfitting due to the small dataset, we adopted data augmentation techniques [46]. Specifically, we applied rotations of angles $\alpha \in 90°, 180°, 270°$ and orthogonal flips to each segmented image to then extract the corresponding rotated versions of $\mathbf{p}_i^t$, s_i^t, r_i^t, and ϕ_i^t for all cells i at each frame t. After computing the required time derivatives, these transformed values were used to enlarge $\mathbf{Y}$ and $\mathbf{D}$ on the LLS problem. Moreover, we worked on normalized data sequences to ensure better-conditioned matrix inversion, prevent feature predominance, and enhance the interpretability of parameters. The data augmentation and the subsequent identification process were performed offline.

The model constants in equations (10), specifically the target area S_{γ_i} and aspect ratio R_{γ_i} with $\gamma_i \in \{\text{MSC}, \text{143b}\}$, were derived directly from dataset statistics regarding mean area and elongation observed across cell trajectories over time (refer to Figure 4). We further analyzed the learned model parameters by examining their distributions across different training sets. This allowed us to evaluate if our open multi-agent model could distinguish between the two cell types (MSC and 143b cells) by capturing their distinct behaviors. The ability to automatically distinguish cells in a co-culture model, such as MSC and osteosarcoma cells, is crucial, as both originate from the same mesenchymal progenitor line and appear morphologically similar under direct microscope observation. Consequently, identifying and analysing cellular behaviours and interactions between these two cell types to gain new insights into cancer progression and aggressiveness is currently limited to systems that are expensive, complex, and often impractical to use.

Specifically, we examined the parameter sets obtained from training on all possible combinations of the four videos, i.e., the power set of the dataset, which consists of 2^4 different training sets. For each training set, we computed the identified parameters and analyzed their statistical distribution using kernel density estimation (KDE) to obtain a smooth approximation of the underlying data distribution. Figure 5 illustrates the KDE-based distribution of the identified parameters for the two

cell types across different training sets. The analysis reveals distinct parameter distributions, supporting the hypothesis that the proposed model effectively differentiates MSC from 143b cells. These differences are more prevalent in parameters associated with repulsion-attraction dynamics ($\theta_{\gamma_i,3}$) and morphological terms ($\theta_{\gamma_i,4}$ and $\theta_{\gamma_i,5}$), highlighting the model capacity to capture biologically relevant heterogeneity in cell behaviors.

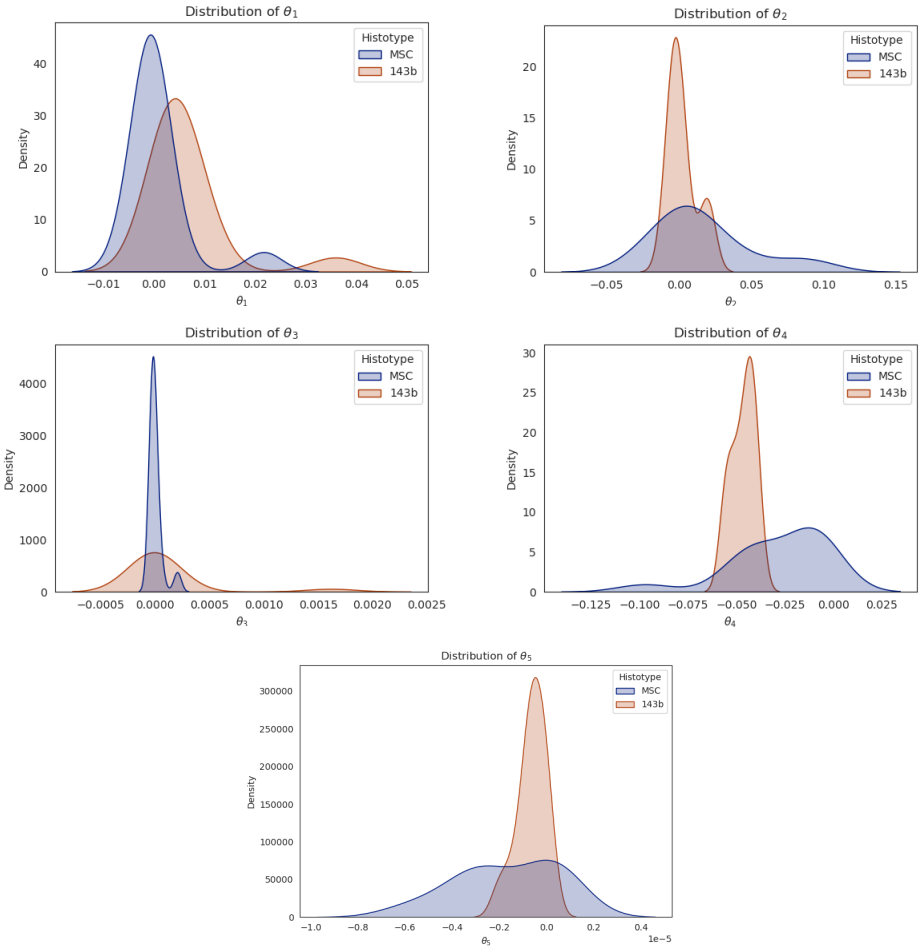

Figure 5: KDE of the identified model parameters for MSC and 143b cells across diverse training sets.

To further detail the tracking algorithm, we now describe the initialization and tuning of the EKF terms used within Algorithm 1. In our implementation of the Extended Kalman Filter, the error covariance matrix $\mathbf{P}^{0|0}$ is initialized by assigning higher variance values to state components that are initially unobserved, reflecting our uncertainty in these estimates. Instead, the measurement covariance matrix $\mathbf{R}$ and the process covariance matrix $\mathbf{Q}$ are set based on baseline estimates obtained from preliminary noise analyses of the dataset. To account for different noise conditions, we further explored scaled versions of these baselines using factors of 0.5, 1.0, and 2.0. This systematic exploration enabled us to quantify the impact of these initialization choices on tracking performance and so identify the optimal settings for our application.

We want to underline that, since our focus is on evaluating the performance metrics of our tracker rather than the detector, we conducted experiments simulating the detection process via gold standard annotations with injected Gaussian disturbances. Specifically, the measurement errors were simulated considering random noise with zero mean and defined covariance for each annotation. In the following, we present some results considering the state format (7) since, being the standard detection format, it enabled us to perform a comparison with other methodologies. Figure 6 shows a video snapshot regarding the numerical experiments on one of the co-culture videos. Here, we display both the bounding boxes predicted by our algorithm and the original gold standard annotations.

We also compared our scheme against a baseline framework in multi-object tracking, namely the Simple Online Real Time Tracking (SORT) algorithm [47]. SORT employs Intersection over Union (IoU) for similarity computation, the Hungarian algorithm for data association, and a standard Kalman filter with single-integrator dynamics for motion prediction. We initialized SORT with the same matrices of Algorithm 1 and simulated the detection process for our proposed solution. The metrics that we chose are the Multiple Object Tracking Accuracy (MOTA) and Multiple Object Tracking Precision (MOTP) [48]. MOTA depends on the number of misses, false positives, and mismatches. MOTP instead compares the predicted bounding boxes

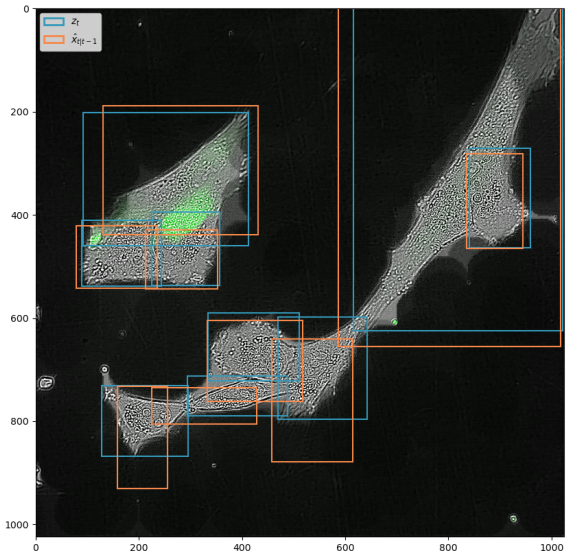

Figure 6: Comparison of predicted bounding boxes and gold standard annotations in a co-culture video frame.

against the real ones. Table I summarizes the results of performing the cross-validation procedure on different experiments, referred to as "Well". This comparison highlights the effectiveness of our approach, as evidenced by a good MOTA score, which reflects the algorithm ability to track cells accurately over time. Furthermore, the MOTP metric demonstrates that the proposed tracking model consistently outperforms SORT, providing more precise predictions.

Table I: Performance comparison

Metric	Cross-Validation on	SORT	Alg. 1
MOTA	Well 1	74.23 %	**83.56 %**
	Well 2	40.78 %	**67.58 %**
	Well 3	76.38 %	**87.02 %**
	Well 4	79.97 %	**96.17 %**
MOTP	Well 1	93.68 %	**96.72 %**
	Well 2	91.45 %	**95.51 %**
	Well 3	93.34 %	**96.03 %**
	Well 4	94.33 %	**97.18 %**

Additionally, the proposed algorithm predicts changes in cell population over time and, at the end of the time-lapse sequence, returns the estimated cell lineage tree $\hat{\mathcal{M}}^t$ for the frames $t \in \{1, \ldots, 172\}$ of the current *in vitro* experiment. Figure 7 shows a prediction result of the latter. Here, the state format in (6) was preferred since it allowed for more precise type discrimination and parent-daughter relation prediction. The depicted example of an estimated cell lineage tree is a reliable result despite the absence of a true reference family tree for direct comparison. In fact, MSC cells rarely divide (considering the duration of the single experiment of about 10 hours), while 143b osteosarcoma cells, due to their oncogenic nature, exhibit a significantly higher mitosis rate. The predicted lineage tree captures these expected proliferation patterns, reinforcing its plausibility.

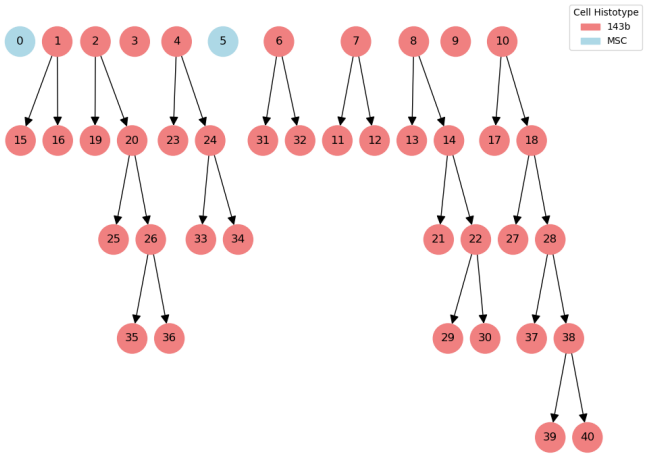

Figure 7: Example of a predicted cell lineage tree.

VI. Conclusions

In this paper we developed a novel algorithm for tracking cells in optical microscopy videos through open multi-agent modeling. System identification techniques applied to *in vitro* experiments enabled to learn cell type-specific parameters, accounting for cell-to-cell interactions even in multi-culture scenarios. The open multi-agent systems framework is the building block of the proposed cell tracking algorithm that is based on a generalized EKF. Cross-validation tests with proper performance metrics were shown together with a comparison with a baseline algorithm in multi-object tracking. Results demonstrate superior effectiveness over state-of-the-art methods in tracking heterogeneous cell types, capturing cell interactions, and generating the cell lineage tree. This study establishes a unique testing framework using a purpose-built dataset obtained from co-culture in vitro experiments with tumor and normal cells.

References

[1] D. Salzano, D. Fiore, and M. di Bernardo, "Ratiometric control for differentiation of cell populations endowed with synthetic toggle switches," in *2019 IEEE 58th Conference on Decision and Control (CDC)*. IEEE, 2019, pp. 927–932.

[2] D. Fiore, D. Salzano, E. Cristòbal-Cóppulo, J. M. Olm, and M. di Bernardo, "Multicellular feedback control of a genetic toggle-switch in microbial consortia," *IEEE Control Systems Letters*, vol. 5, no. 1, pp. 151–156, 2020.

[3] C. Romano, A. Borri, and M. D. Di Benedetto, "Stackelberg evolutionary games for cancer modeling and treatment," in *2024 IEEE 63rd Conference on Decision and Control (CDC)*. IEEE, 2024, pp. 7044–7049.

[4] M. Khammash, M. Di Bernardo, and D. Di Bernardo, "Cybergenetics: Theory and methods for genetic control system," in *2019 IEEE 58th Conference on Decision and Control (CDC)*. IEEE, 2019, pp. 916–926.

[5] T. E. Gorochowski, A. Matyjaszkiewicz, T. Todd, N. Oak, K. Kowalska, S. Reid, K. T. Tsaneva-Atanasova, N. J. Savery, C. S. Grierson, and M. Di Bernardo, "Bsim: an agent-based tool for modeling bacterial populations in systems and synthetic biology," *PLoS ONE*, 2012.

[6] J. Mason and D. Öhlund, "Key aspects for conception and construction of co-culture models of tumor-stroma interactions," *Frontiers in Bioengineering and Biotechnology*, vol. 11, p. 1150764, 2023.

[7] E. J. Sutton, T. D. Henning, B. J. Pichler, C. Bremer, and H. E. Daldrup-Link, "Cell tracking with optical imaging," *European Radiology*, vol. 18, pp. 2021–2032, 2008.

[8] H.-J. Cheng, C.-H. Hsu, C.-L. Hung, and C.-Y. Lin, "A review for cell and particle tracking on microscopy images using algorithms and deep learning technologies," *Biomedical Journal*, vol. 45, no. 3, pp. 465–471, 2022.

[9] V. Ulman, M. Maška, K. E. Magnusson, O. Ronneberger, C. Haubold, N. Harder, P. Matula, P. Matula, D. Svoboda, M. Radojevic *et al.*, "An objective comparison of cell-tracking algorithms," *Nature Methods*, vol. 14, no. 12, pp. 1141–1152, 2017.

[10] M. Maška, V. Ulman, P. Delgado-Rodriguez, E. Gómez-de Mariscal, T. Nečasová, F. A. Guerrero Peña, T. I. Ren, E. M. Meyerowitz, T. Scherr, K. Löffler *et al.*, "The cell tracking challenge: 10 years of objective benchmarking," *Nature Methods*, pp. 1–11, 2023.

[11] Y. Chen, Y. Song, C. Zhang, F. Zhang, L. O'Donnell, W. Chrzanowski, and W. Cai, "Celltrack r-cnn: A novel end-to-end deep neural network for cell segmentation and tracking in microscopy images," in *2021 IEEE 18th International Symposium on Biomedical Imaging (ISBI)*. IEEE, 2021, pp. 779–782.

[12] J. C. Kimmel, A. S. Brack, and W. F. Marshall, "Deep convolutional and recurrent neural networks for cell motility discrimination and prediction," *IEEE/ACM Transactions on Computational Biology and Bioinformatics*, vol. 18, no. 2, pp. 562–574, 2019.

[13] D. E. Hernandez, S. W. Chen, E. E. Hunter, E. B. Steager, and V. Kumar, "Cell tracking with deep learning and the viterbi algorithm," in *IEEE International Conference on Manipulation, Automation and Robotics at Small Scales*, 2018, pp. 1–6.

[14] H. Hu, L. Zhou, Q. Guan, Q. Zhou, and S. Chen, "An automatic tracking method for multiple cells based on multi-feature fusion," *IEEE Access*, vol. 6, pp. 69 782–69 793, 2018.

[15] T. Ben-Haim and T. R. Raviv, "Graph neural network for cell tracking in microscopy videos," in *European Conference on Computer Vision*. Springer, 2022, pp. 610–626.

[16] K. Löffler and R. Mikut, "Embedtrack—simultaneous cell segmentation and tracking through learning offsets and clustering bandwidths," *IEEE Access*, vol. 10, pp. 77 147–77 157, 2022.

[17] O. Hirose, S. Kawaguchi, T. Tokunaga, Y. Toyoshima, T. Teramoto, S. Kuge, T. Ishihara, Y. Iino, and R. Yoshida, "Spf-celltracker: Tracking multiple cells with strongly-correlated moves using a spatial particle filter," *IEEE/ACM Transactions on Computational Biology and Bioinformatics*, vol. 15, no. 6, pp. 1822–1831, 2017.

[18] F. Boukari and S. Makrogiannis, "Automated cell tracking using motion prediction-based matching and event handling," *IEEE/ACM Transactions on Computational Biology and Bioinformatics*, vol. 17, no. 3, pp. 959–971, 2018.

[19] T. E. Gorochowski, S. Hauert, J.-U. Kreft, L. Marucci, N. R. Stillman, T.-Y. D. Tang, L. Bandiera, V. Bartoli, D. O. Dixon, A. J. Fedorec *et al.*, "Toward engineering biosystems with emergent collective functions," *Frontiers in Bioengineering and Biotechnology*, vol. 8, p. 705, 2020.

[20] P. Mina, K. Tsaneva-Atanasova, and M. d. Bernardo, "Entrainment and control of bacterial populations: an in silico study over a spatially extended agent based model," *ACS Synthetic Biology*, vol. 5, no. 7, pp. 639–653, 2016.

[21] S. Izumi, S.-I. Azuma, and T. Sugie, "Multi-robot control inspired by bacterial chemotaxis: coverage and rendezvous via networking of chemotaxis controllers," *IEEE Access*, vol. 8, pp. 124 172–124 184, 2020.

[22] A. Mironchenko, "Live systems of varying dimension: modeling and stability," in *2023 62nd IEEE Conference on Decision and Control (CDC)*. IEEE, 2023, pp. 3956–3961.

[23] H. Enderling and M. AJ Chaplain, "Mathematical modeling of tumor growth and treatment," *Current Pharmaceutical Design*, vol. 20, no. 30, pp. 4934–4940, 2014.

[24] V. Martinelli, D. Salzano, D. Fiore, and M. di Bernardo, "Multicellular pi control for gene regulation in microbial consortia," *IEEE Control Systems Letters*, vol. 6, pp. 3373–3378, 2022.

[25] A. Guarino, D. Fiore, D. Salzano, and M. di Bernardo, "Balancing cell populations endowed with a synthetic toggle switch via adaptive pulsatile feedback control," *ACS Synthetic Biology*, vol. 9, no. 4, pp. 793–803, 2020.

[26] C. Romano, A. Borri, and M. D. Di Benedetto, "Adaptive responses of cancer cells to tumor microenvironment changes: an evolutionary model perspective," in *2024 IEEE 20th International Conference on Automation Science and Engineering (CASE)*. IEEE, 2024, pp. 2079–2084.

[27] H. Jiao, Q. Shen, Y. Shi, and P. Shi, "Adaptive tracking control for uncertain cancer-tumor-immune systems," *IEEE/ACM Transactions on Computational Biology and Bioinformatics*, vol. 18, no. 6, pp. 2753–2758, 2020.

[28] L. Von Bertalanffy, "The theory of open systems in physics and biology," *Science*, vol. 111, no. 2872, pp. 23–29, 1950.

[29] H. Oh, A. R. Shirazi, C. Sun, and Y. Jin, "Bio-inspired self-organising multi-robot pattern formation: A review," *Robotics and Autonomous Systems*, vol. 91, pp. 83–100, 2017.

[30] M. Cortini, S. Avnet, and N. Baldini, "Mesenchymal stroma: role in osteosarcoma progression," *Cancer Letters*, vol. 405, pp. 90–99, 2017.

[31] S. Avnet, G. Di Pompo, T. Chano, C. Errani, A. Ibrahim-Hashim, R. J. Gillies, D. M. Donati, and N. Baldini, "Cancer-associated mesenchymal stroma fosters the stemness of osteosarcoma cells in response to intratumoral acidosis via nf-κb activation," *International journal of cancer*, vol. 140, no. 6, pp. 1331–1345, 2017.

[32] S. Avnet, S. Lemma, M. Cortini, G. Di Pompo, F. Perut, M. V. Lipreri, L. Roncuzzi, M. Columbaro, C. Errani, A. Longhi *et al.*, "The release of inflammatory mediators from acid-stimulated mesenchymal stromal cells favours tumour invasiveness and metastasis in osteosarcoma," *Cancers*, vol. 13, no. 22, p. 5855, 2021.

[33] C. Massaro, H. N. Sensoy, M. Mulders, C. De Schrijver, C. Gómez-Martín, J. Simon Nieto, T. Lagerweij, A. Atmopawiro, J. Pérez-Boza, M. Bebelman *et al.*, "Tumor-secreted extracellular vesicles counteract therapy response by triggering inflammatory mesenchymal stem cell development," *Clinical Cancer Research*, vol. 30, no. 20, pp. 4714–4728, 2024.

[34] A. Tramaloni, A. Testa, S. Avnet, N. Baldini, and G. Notarstefano, "Biological cell tracking via multi-agent identification and filtering," in *2024 IEEE 63rd Conference on Decision and Control (CDC)*. IEEE, 2024, pp. 1338–1343.

[35] G. Ciaparrone, F. L. Sánchez, S. Tabik, L. Troiano, R. Tagliaferri, and F. Herrera, "Deep learning in video multi-object tracking: A survey," *Neurocomputing*, vol. 381, pp. 61–88, 2020.

[36] H. Sayama, "Swarm chemistry," *Artificial Life*, vol. 15, no. 1, pp. 105–114, 2009.

[37] M. Eyiyurekli, L. Bai, P. I. Lelkes, and D. E. Breen, "Chemotaxis-based sorting of self-organizing heterotypic agents," in *ACM Symposium on Applied Computing*, 2010, pp. 1315–1322.

[38] S. L. Brunton, J. L. Proctor, and J. N. Kutz, "Discovering governing equations from data by sparse identification of nonlinear dynamical systems," *Proceedings of the national academy of sciences*, vol. 113, no. 15, pp. 3932–3937, 2016.

[39] R. E. Kalman, "A new approach to linear filtering and prediction problems," *Journal of Basic Engineering*, vol. 82, no. 1, pp. 35–45, 1960.

[40] H. Rezatofighi, N. Tsoi, J. Gwak, A. Sadeghian, I. Reid, and S. Savarese, "Generalized intersection over union: A metric and a loss for bounding box regression," in *IEEE/CVF Conference on Computer Vision and Pattern Recognition*, 2019, pp. 658–666.

[41] H. W. Kuhn, "The hungarian method for the assignment problem," *Naval Research Logistics Quarterly*, vol. 2, no. 1-2, pp. 83–97, 1955.

[42] G. Bradski, A. Kaehler *et al.*, "Opencv," *Dr. Dobb's Journal of Software Tools*, vol. 3, no. 2, 2000.

[43] E. Pedone, I. De Cesare, C. G. Zamora-Chimal, D. Haener, L. Postiglione, A. La Regina, B. Shannon, N. J. Savery, C. S. Grierson, M. Di Bernardo *et al.*, "Cheetah: a computational toolkit for cybergenetic control," *ACS Synthetic Biology*, vol. 10, no. 5, pp. 979–989, 2021.

[44] C. Stringer, T. Wang, M. Michaelos, and M. Pachitariu, "Cellpose: a generalist algorithm for cellular segmentation," *Nature methods*, vol. 18, no. 1, pp. 100–106, 2021.

[45] M. Stone, "Cross-validatory choice and assessment of statistical predictions," *Journal of the royal statistical society: Series B (Methodological)*, vol. 36, no. 2, pp. 111–133, 1974.

[46] A. Mumuni and F. Mumuni, "Data augmentation: A comprehensive survey of modern approaches," *Array*, vol. 16, p. 100258, 2022.

[47] A. Bewley, Z. Ge, L. Ott, F. Ramos, and B. Upcroft, "Simple online and realtime tracking," in *IEEE International Conference on Image Processing*, 2016, pp. 3464–3468.

[48] K. Bernardin and R. Stiefelhagen, "Evaluating multiple object tracking performance: the clear mot metrics," *EURASIP Journal on Image and Video Processing*, vol. 2008, pp. 1–10, 2008.

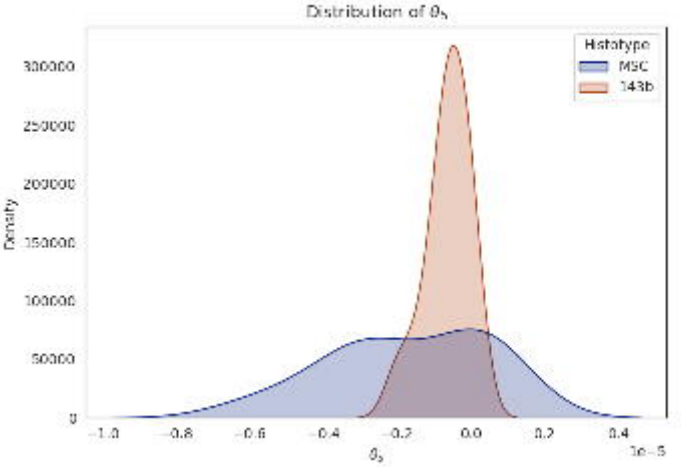
Distribution of θ_5
Histotype
MSC
143b
Density
300000
250000
200000
150000
100000
50000
0
−1.0
−0.8
−0.6
−0.4
−0.2
0.0
0.2
0.4
θ_5
1e−5

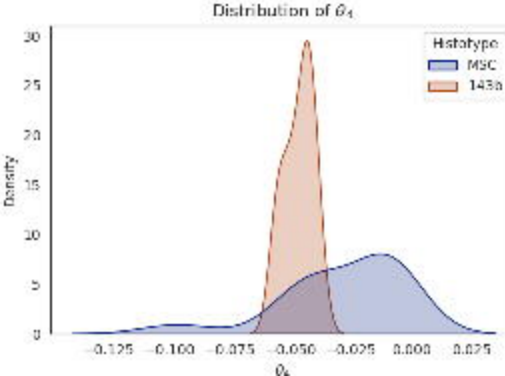
Distribution of θ_4
Histotype
MSC
143b
Density
30
25
20
15
10
5
0
−0.125
−0.100
−0.075
−0.050
−0.025
0.000
0.025
θ_4

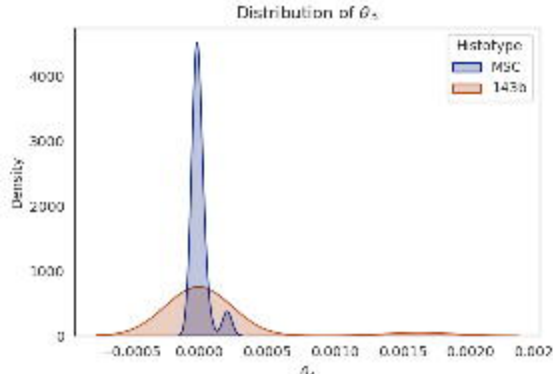
Distribution of θ_4
Histotype
MSC
143b
Density
4000
3000
2000
1000
0
−0.0005
0.0000
0.0005
0.0010
0.0015
0.0020
0.0025
θ_4

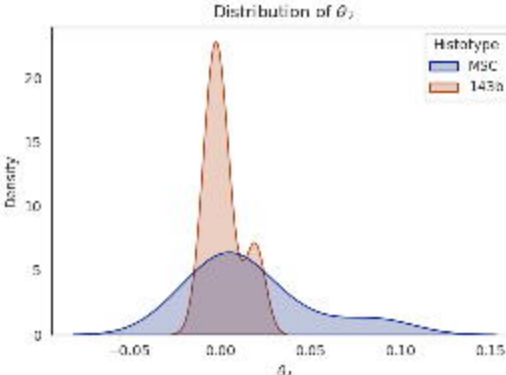
Distribution of θ_i
Histotype
MSC
143b
Density
20
15
10
5
0
−0.05
0.00
0.05
0.10
0.15
θ_i

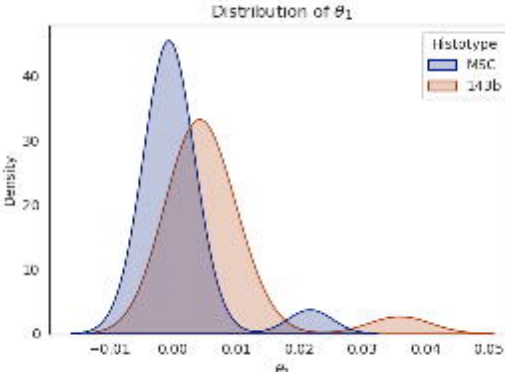
Distribution of θ_1
Histotype
MSC
140b
Density
40
30
20
10
0
−0.01
0.00
0.01
0.02
0.03
0.04
0.05
θ_1

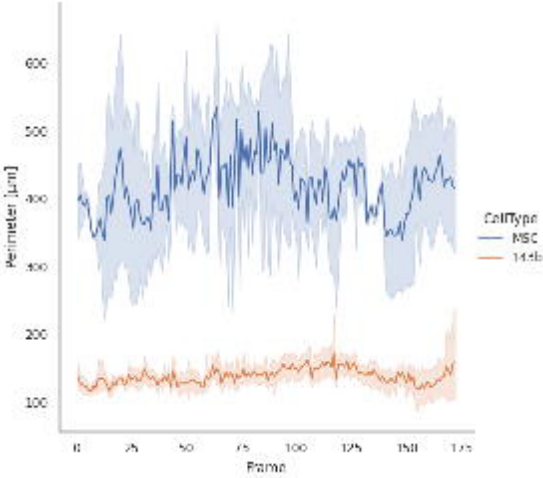
600
500
400
300
200
100
Perimeter [µm]
0
25
50
75
100
125
150
175
Frame
CellType
MSC
144b

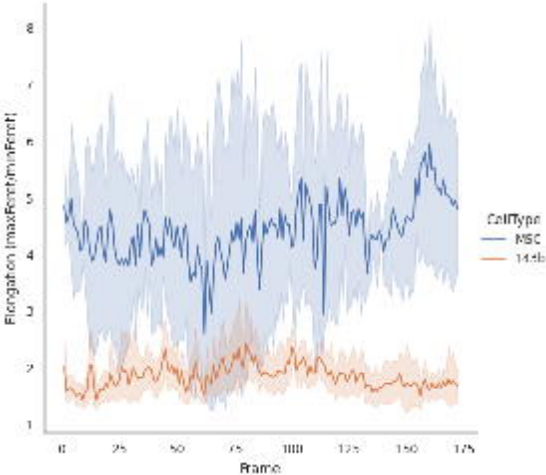
Elongation (max/min)
8
7
6
5
4
3
2
1
0
25
50
75
100
125
150
175
Frame
CellType
MSC
144b

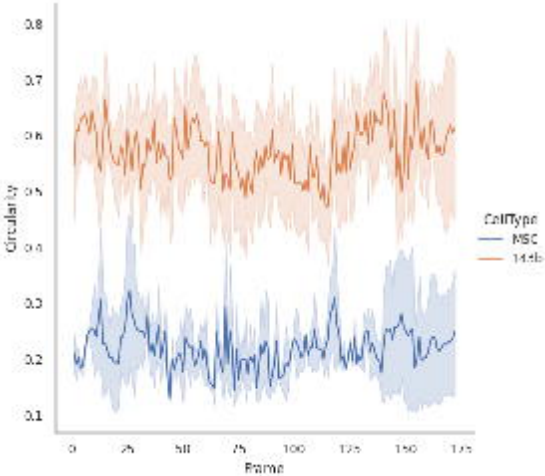
0.8
0.7
0.6
0.5
0.4
0.3
0.2
0.1
Circularity
0
25
50
75
100
125
150
175
Frame
CellType
MSC
14sb

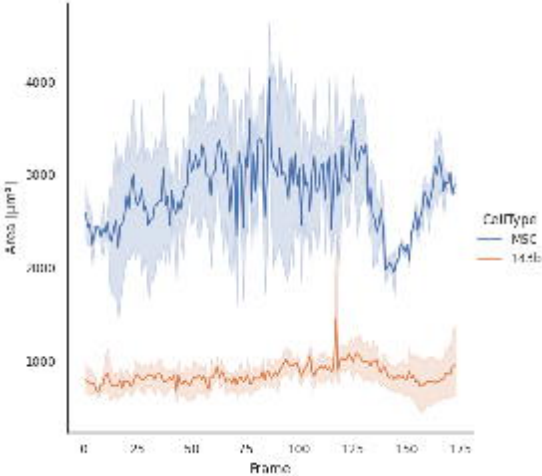
4000
3000
2000
1000
Area [µm²]
0
25
50
75
100
125
150
175
Frame
CellType
MSC
14db

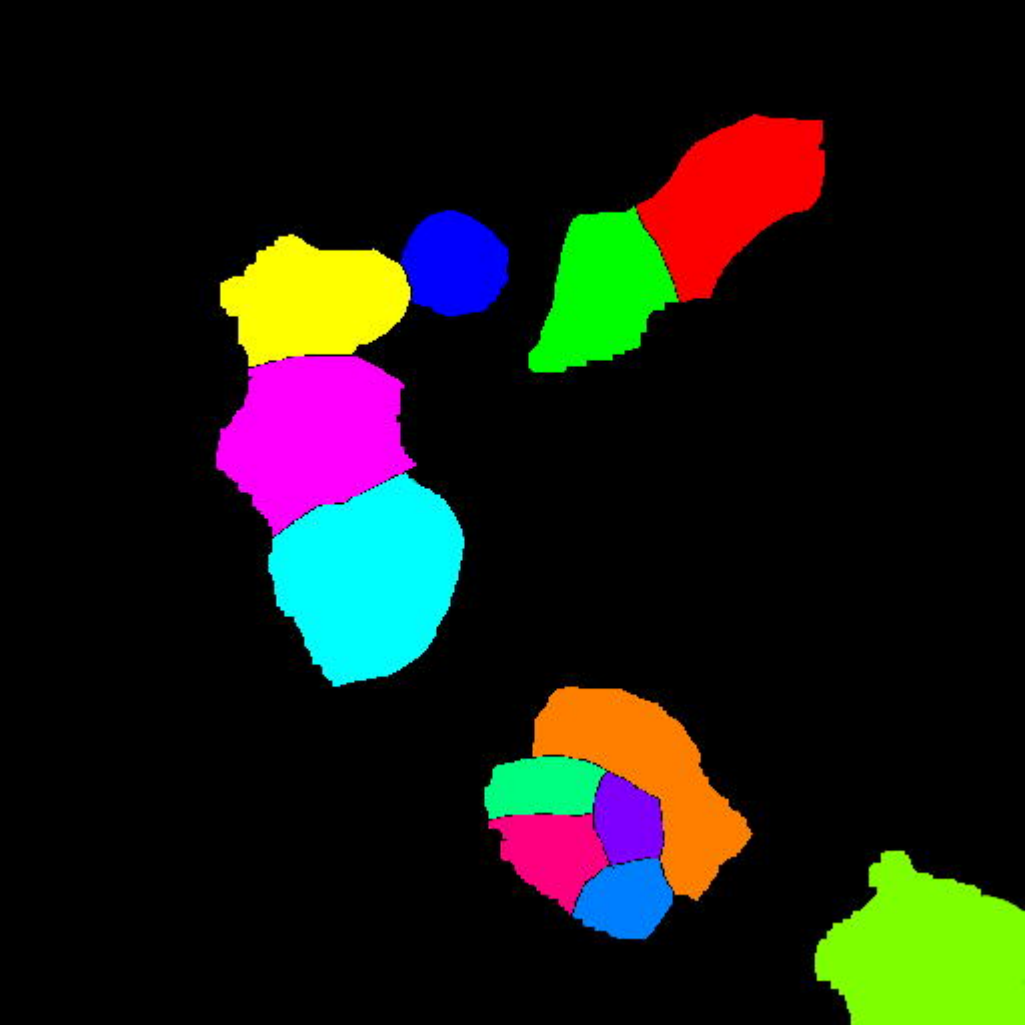

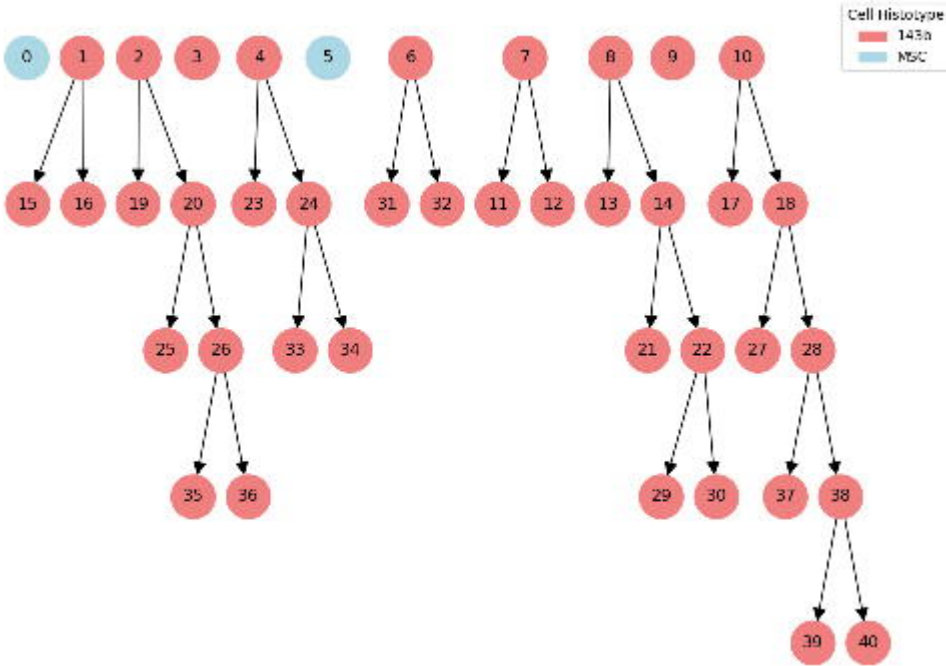
Cell Histotype
143b
MSC
0
1
2
3
4
5
6
7
8
9
10
15
16
19
20
23
24
31
32
11
12
13
14
17
18
25
26
33
34
21
22
27
28
35
36
29
30
37
38
39
40

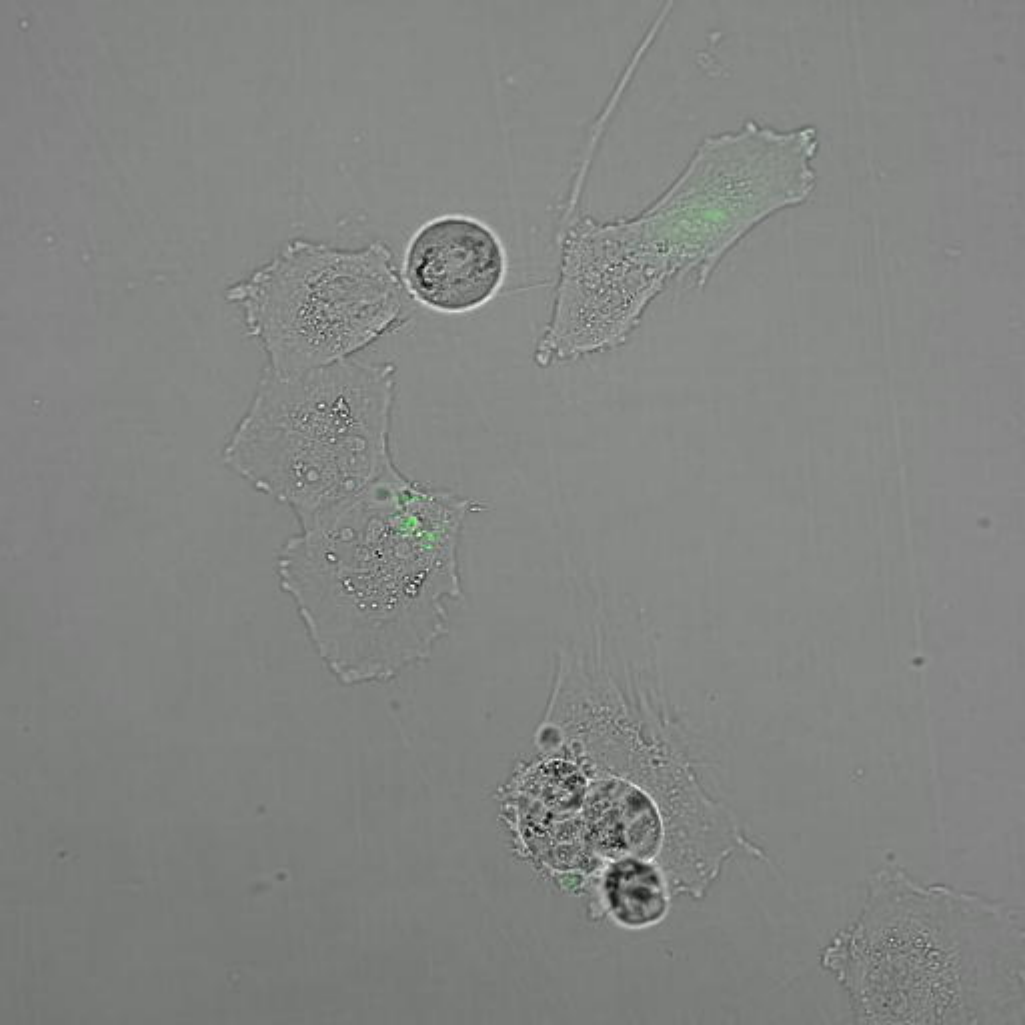

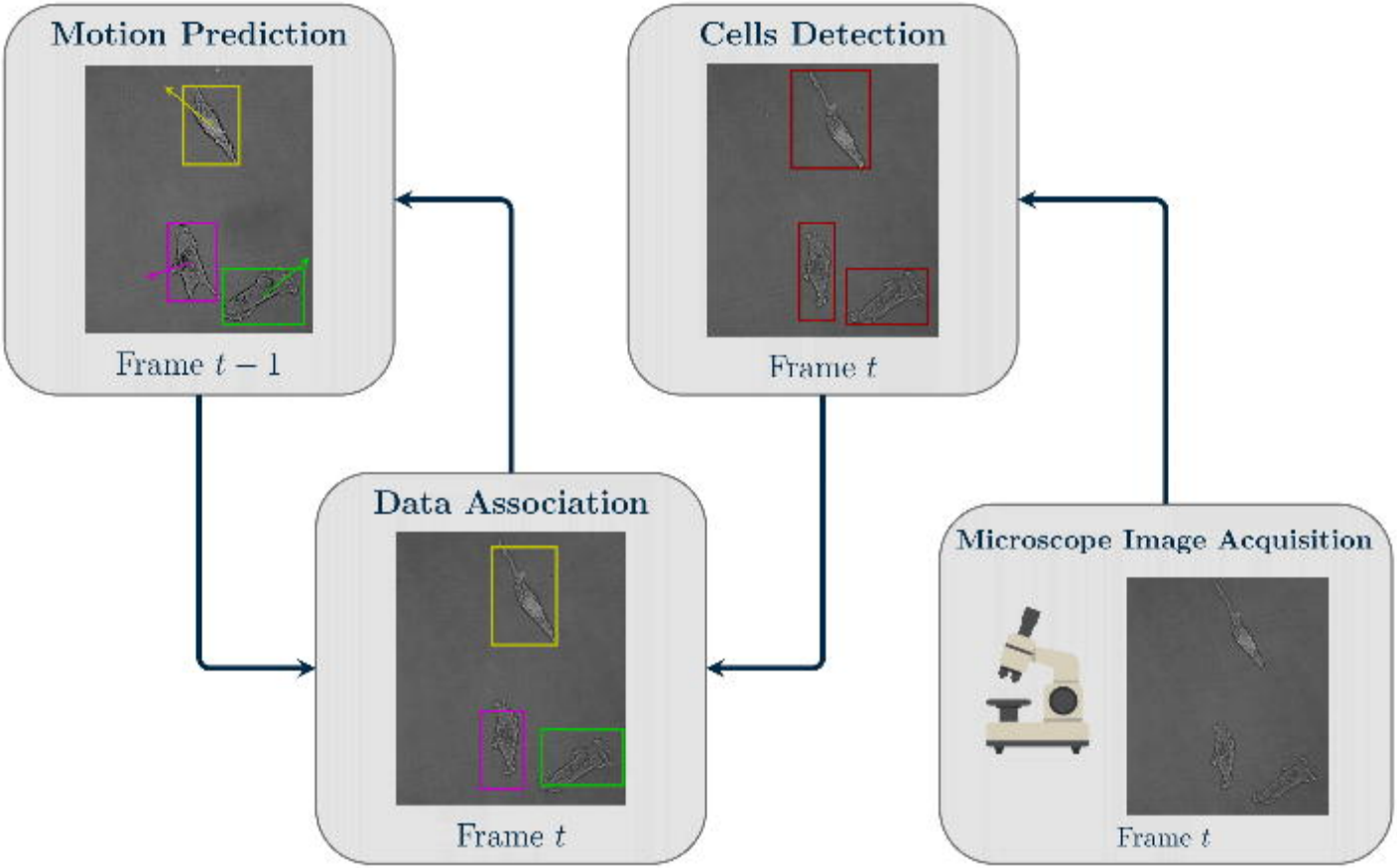
Motion Prediction
Frame $t-1$
Cells Detection
Frame t
Data Association
Frame t
Microscope Image Acquisition
Frame t

$L_p^{t-1} = L_d^{t-1} = L_{\text{IN}}^{t-1} = L_{\text{OUT}}^{t-1} = \emptyset$

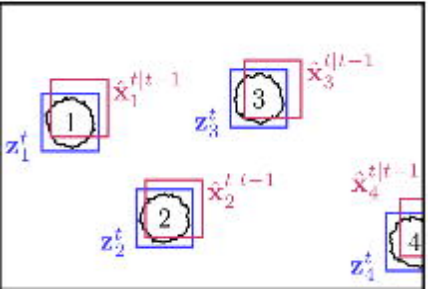

$L_p^t = \{1\}, L_d^t = \{(5,6)_1\}, L_{\text{OUT}}^t = \{1\}$

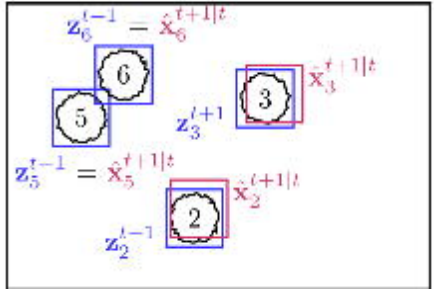

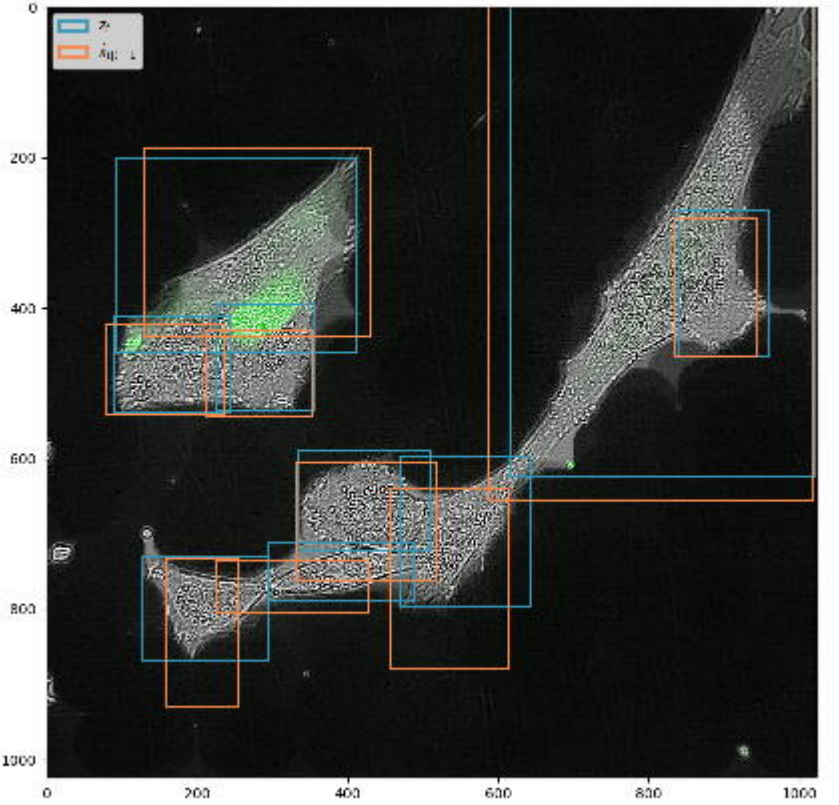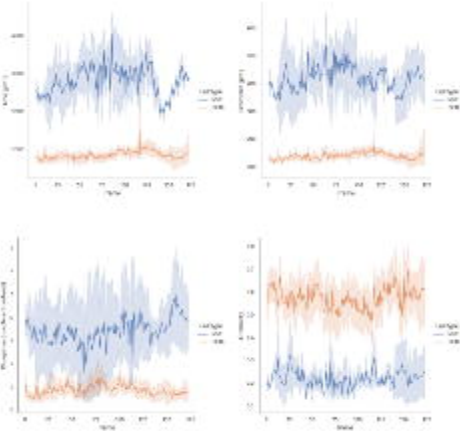
0
200
400
600
800
1000
0
200
400
600
800
1000